



# The boundary-layer characteristics and unsteady flow topology of full-scale operational inter-modal freight trains

J.R. Bell<sup>a,b,\*</sup>, D. Burton<sup>a</sup>, M.C. Thompson<sup>a</sup>

<sup>a</sup> Department of Mechanical and Aerospace Engineering, Monash University, Clayton, Victoria, Australia

<sup>b</sup> German Aerospace Center (DLR), Institute for Aerodynamics and Flow Technology (AS), Göttingen, Germany

## ARTICLE INFO

### Keywords:

Freight train  
Transient flow  
Induced flow  
Boundary layer  
Real-world conditions  
Train aerodynamics

## ABSTRACT

The boundary layers that develop at the sides of full-scale operational inter-modal freight trains were measured using rakes of 4-hole dynamic-pressure probes. The average boundary-layer displacement thickness at the middle of the trains measured under low crosswind was 1.6 m (within the range of 0.5–3 m), showing turbulence intensities of 4–13%, and length scales of 5–30 m. These characteristics, together with other quantitative details provided in the paper, are intended to provide insight for future experiments and simulations to model real-world conditions around freight trains. The sensitivity of the boundary layer and flow topology to environmental crosswinds and loading configuration was also investigated. In addition, insight is provided into the unsteady flow topology around freight trains, the frequency content of the induced flow, and correlation characteristics.

## 1. Introduction

Inter-modal freight trains in typical operation have lengths of up to 1.6 km, carry a variety of freight container sizes, and travel at up to 110 km/h. The various container sizes can be double-stacked during transport, as well as carried via different wagon types, resulting in a loading configuration where horizontal gap length and height are variables with a significant range that vary along the length of the train. Efforts are made in practice to optimize the loading configuration for weight distribution and volume efficiency. However, operational conditions also have clear scope for aerodynamic optimization that is not often realised in practice.

The aerodynamics of freight trains are important for the vehicle's overall resistance and, therefore, efficiency. Aerodynamic resistance (drag) can be significantly greater than rolling resistance (Raghuathan et al., 2002; Shetz, 2001). This is primarily due to the steel wheel-rail interface resulting in low rolling resistance and in contrast, the high aerodynamic resistance that arises from the overall make-up of the vehicle; a collection of a number of predominantly bluff components connected in series. In addition, the crosswind stability of a train and its components are a critical aerodynamic characteristic that concerns the safety of the operators, as well as nearby civilians and infrastructure. Thus, there has been significant research into the aerodynamics of freight trains, with full-scale experiments (Lai and Barkan, 2005; Lai et al., 2008;

Lukaszewicz, 2007, 2009; Gallagher et al., 2018), scaled wind-tunnel experiments (Li et al., 2017; Watkins et al., 1992; Engdahl et al., 1986; Gielow and Furlong, 1988; Storms et al., 2008; Peters, 1993), scaled moving-model experiments (Soper et al., 2014) and Computational Fluid Dynamic (CFD) simulations (Östh & Krajnović 2014; Maleki et al., 2017, 2019; Flynn et al., 2014, 2016; Hemida and Baker, 2010; Gallagher et al., 2018; Paul et al., 2007) having been performed. Such research has established that there exists scope for aerodynamic optimization of these vehicles. Recommendations for improved aerodynamic loading configurations have been made (Li et al., 2017; Lai et al., 2008; Lai and Barkan, 2005; Beagles and Fletcher, 2013; Engdahl et al., 1986; Paul et al., 2007), as well as design considerations of containers and wagons (Watkins et al., 1992; Öngüner et al., 2020). Further, insight into the flow field around these vehicles (Östh and Krajnović, 2014, Soper, 2014; Li et al., 2017; Maleki et al., 2017, 2019) have provided insight into the causal mechanisms of the forces experienced.

Accommodating the operational length to height ratios ( $L/H = 250\text{--}500$ ) is a significant difficulty in accurately modelling the realistic aerodynamic conditions around a freight train. This difficulty arises from physical limitations in scaled experiments (for example, wind-tunnel test-section length) and computational resource requirements in numerical simulations. This often results in considerably reduced train lengths being modelled ( $L/H = 10\text{--}50$ ). This difficulty and the induced effects have been acknowledged and considered in high-speed train aero-

\* Corresponding author. Department of Mechanical and Aerospace Engineering, Monash University, Clayton, Victoria, Australia.  
E-mail address: [james.bell@dlr.de](mailto:james.bell@dlr.de) (J.R. Bell).

dynamic investigations, where comparatively moderate length to height ratios ( $L/H = 25\text{--}100$ ) exist (Mulder et al., 2013; Bell et al., 2017, 8–11 December, 2014). Beyond the local flow topology that occurs around the head of the train, (and similarly, prior to the local flow around the tail), a boundary layer develops over the surface of the vehicle. The developing boundary layer is characterised by the velocity, turbulence and length-scale profiles.

The aerodynamic characteristics of bluff bodies and their geometric features in general have been well established to be sensitive to the turbulent conditions they are exposed to (Cooper and Campbell, 1981; Watkins and Cooper, 2007). In wind engineering, accurate modelling of the velocity, turbulence and length-scale atmospheric boundary-layer characteristics that a building is exposed to is critical for ensuring accurate prediction of wind loads (Holmes, 2001). Similarly, there have been recent efforts to characterise (Wordley and Saunders, 2008; McAuliffe et al., 2014) real-world on-road turbulence and replicate these conditions in wind-tunnel and CFD simulations for automotive aerodynamic investigations (Sims-Williams, 2011). Specifically, the aerodynamic sensitivity of a freight container to the conditions it is exposed to has been indicated by a number of investigations. A container in isolation has been shown to experience a significantly different flow field, pressure distribution and forces to a container located within a series of containers (Östth and Krajnovic', 2014, Li et al., 2017; Maleki et al., 2017, 2019). Further, the drag of individual containers have reportedly been found to be dependent on location in the train, only becoming consistent at approximately 8 cars from the nose (Gielow and Furlong, 1988; Engdahl et al., 1986). Thus, there is clear motivation to accurately represent the flow that a shipping container is exposed to, in order to ensure that the findings from investigations aiming for optimization are correct in their magnitude and overall effect.

A common method in investigations that consider the effect that model length can have on aerodynamic findings, is to model an arbitrary region within the length of the train, representative of the conditions that the majority of containers experience (Östth and Krajnovic', 2014, Li et al., 2017; Maleki et al., 2017, 2019). However, the characteristics at this arbitrary *middle* position, until now, have not been defined for operational freight trains subject to real-world atmospheric conditions. Some insight into these characteristics has been limited to slipstream-motivated experimental campaigns, which are focussed on accurately measuring the peak induced-velocity caused by trains at a specific position in their immediate vicinity (3 m from the track centre); where waiting passengers, workers or infrastructure can be most strongly affected. With safety as a motivation, and the resulting European regulations for testing and requirements that must be met for trains to operate (CEN, 2013), there has been a wide range of research in the area (Sterling et al., 2008; Soper et al., 2014; Mulder et al., 2013; Flynn et al., 2014, 2016; Bell et al., 8–11 December, 2014; 2016b; 2017; Soper and Baker, 2019). However, such research and regulations are not intended to, and therefore do not properly measure and resolve a train's boundary-layer characteristics.

With further insight into the boundary layer characteristics of operational freight trains, models in future investigations could be tuned to match realistic oncoming conditions in the same manner as for the atmospheric boundary layer in the practice of wind engineering. Experimentally, this could be achieved through boundary-layer augmentation utilizing roughness, tripping and vortex-generating elements (Irwin, 1981, Bell et al., 8–11 December, 2014, Sima et al., 2016; Buhr and Ehrenfried, 2017; Bell et al., 2017). Similar approaches could be applied numerically, or alternatively, through advanced recycling techniques (Östth and Krajnovic', 2014) or through tuning of inlet conditions.

In this work, the characteristics of boundary layers of operational inter-modal freight trains are presented. Here we use the terminology *boundary layer* in a broad sense to describe the induced flow along the side of the train and tracks. It may be a combination of turbulent structures generated along the side of the train, and, in the presence of cross-wind, wake structures over the side of the train. Measurements were

made with 3 horizontal boundary-layer rakes perpendicular to the rail to measure the side boundary-layer. Each rake contained 7 four-hole dynamic pressure probes. A vertical rake of 3 probes was also utilized to investigate the boundary layer's three-dimensionality. In addition to quantifying the boundary layers, insight into the flow physics around inter-modal shipping containers and their loading configurations is presented.

Measurements of six inter-modal freight trains were performed, each effectively measured three times by each of the horizontal rakes. Inter-modal freight trains have no standard, consistent configuration. Therefore, each train had different loading configurations and further, operated within different environmental conditions. It is acknowledged this is a small sample size that does not result in a statistically significant description of a benchmark-type boundary-layer for a specific train. However, these measurements — for the first time — enable the boundary layer characteristics representative of real, inter-modal freight trains operating in real conditions to be described. These results provide valuable insight into real-world operational conditions and hence can be used to help inform setting up wind-tunnel experiments and numerical simulations that investigate the aerodynamics of freight trains. This work is part of a collaboration with Pacific National — a freight transport provider — with the ultimate aim of improving the aerodynamic efficiency of inter-modal freight transport.

## 2. Methodology

### 2.1. Test site

The experiment was performed at Wingeel, Victoria, Australia. The standard-gauge track network that inter-modal freight trains operated within proximity to Melbourne was assessed for aerodynamic and logistical considerations. The Wingeel test site was identified as suitable, utilizing Pacific Nationals expertise as a transport operators.

The test site consisted (Fig. 1) of a single track, which allowed access and simultaneous measurement along both sides of the train without having to consider rail traffic on a parallel track. Trains operate at full operational speed ( $u_t \approx 110$  km/hr) and were given prior notice of the experiment and infrastructure setup to maintain the maximum speed during passage past the data collection infrastructure. The track is relatively straight (Fig. 2), which enabled a straight vehicle passing the measurement equipment to operate at maximum speed.

A minor highway was located approximately 1 km north of the test site. At this distance, the effect of passing automotive vehicles on the measurements was expected to be negligible. A minor local road crossed the railway 50 m east of the test site and contained minimal traffic infrastructure (lights/sirens) mounted on poles. This road experienced minimal traffic, and vehicles if present were stationary and  $\approx 10$  m from the track during measurements of the trains. This configuration is not expected to have significantly shielded the measurement devices from the induced flow of the trains being measured, and thus not expected to have a significant influence on the results.

The local topography was relatively flat, and clear of trees and vegetation. Minimal local topography was desired, to best represent the ideal conditions of the rail vehicle operating in open air. This of course opened the site and vehicle to be exposed to ambient wind, however, those conditions were measured.

### 2.2. Test vehicles & conditions

The passing of inter-modal freight trains in normal operation were recorded in the experiment. Only single-stacked shipping containers existed on the trains subject to measurement. A variety of loading configurations, in terms of gap sizes between containers, existed within each train measured, and indeed between all trains in the set. In Fig. 3, the extent of gap variation is visible. Fig. 3(a) illustrates how containers can be positioned with no gap between them when loaded on the same



Fig. 1. An operational full-scale inter-modal freight train driving past measurement rakes of 4-hole dynamic pressure probes, placed either side of the train.

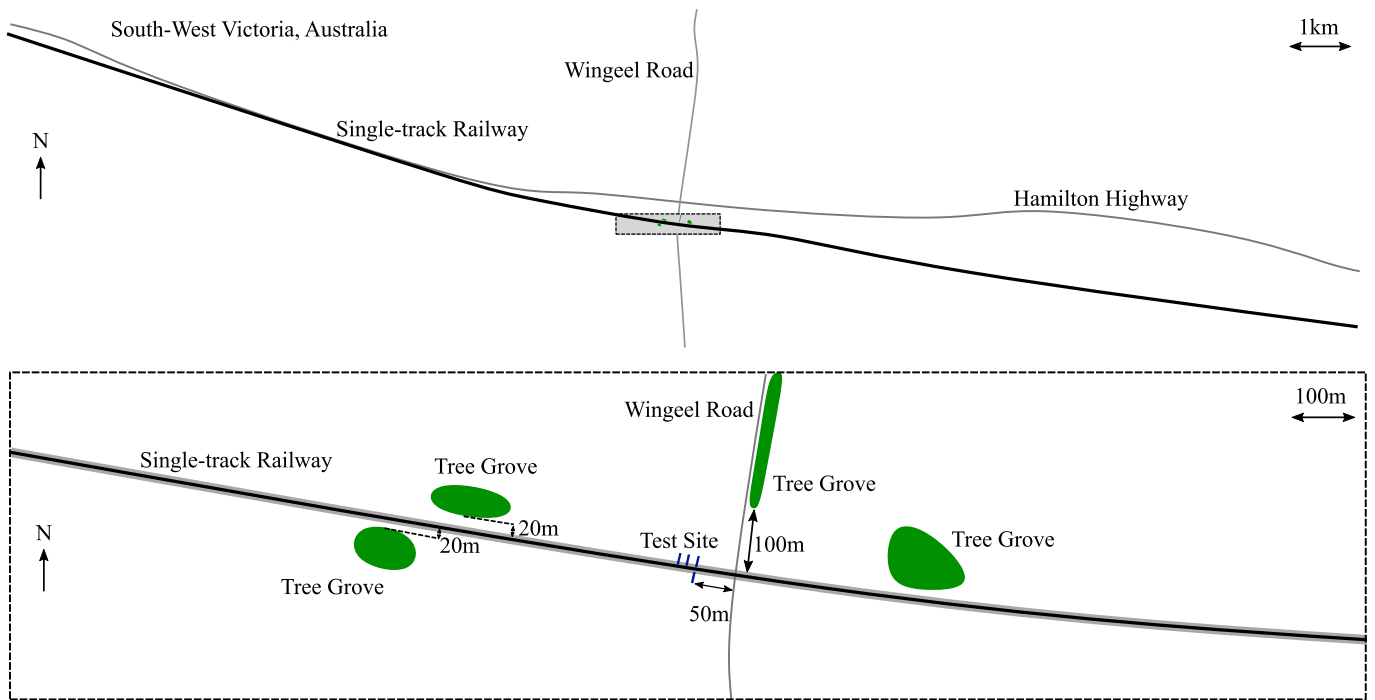


Fig. 2. The experiment test site at Wingeel, Victoria, Australia. A large-scale view of the track and roads are illustrated (top), with the local topography and location of trees and vegetation illustrated in the zoomed-in figure inset below.

wagon. Also in Fig. 3(a, a) small gap is visible that is required when containers are loaded on sequential wagons, due to the distance required by the coupling between wagons which also provides the ability for the train to operate through curves. In Fig. 3(b, a) ‘fractional’ gap is visible. These occur due to the mismatch between available space on the wagon for loading, and the size of the container(s) loaded onto this space (referred to as slot utilization). In Fig. 3c and d, gaps in the order of a full sized container or larger are visible. These occur as it is common practice for sets (typically of 5) of multiple wagons to be grouped and moved together. When these groups are loaded and added to make a full train, such gaps can exist due to un-required or unsuitable space on the wagon for more containers.

In this experiment, 6 inter-modal trains were measured. The train number, loading configuration description (quantified loading configuration is presented in Section 3.2), and test conditions: train speed  $u_t$ , ambient wind speed,  $u_a$ , absolute ambient-wind yaw-angle  $\gamma$ , and relative

ambient-wind yaw-angle  $\beta$  (both angles being around the z-axis), are presented in Table 1. The effects of these characteristics are discussed in the results section.

### 2.3. Setup

The measurement equipment was arranged at the Wingeel site and measurements were obtained as the trains passed by them as presented in Fig. 1. The experimental setup of the measurement equipment and data acquisition is illustrated in Fig. 4, with photos of the setup and specific equipment provided in Fig. 5.

The primary pieces of measurement equipment were 4-hole dynamic-pressure probes, positioned in three rakes (R1, R2 & R4 in Fig. 4) of 7 probes, arranged perpendicular to the path of the trains. The probe nearest to the train was located 2.5 m from the nearest rail, which corresponds to  $y = 1.71$  m from the surface of a shipping container

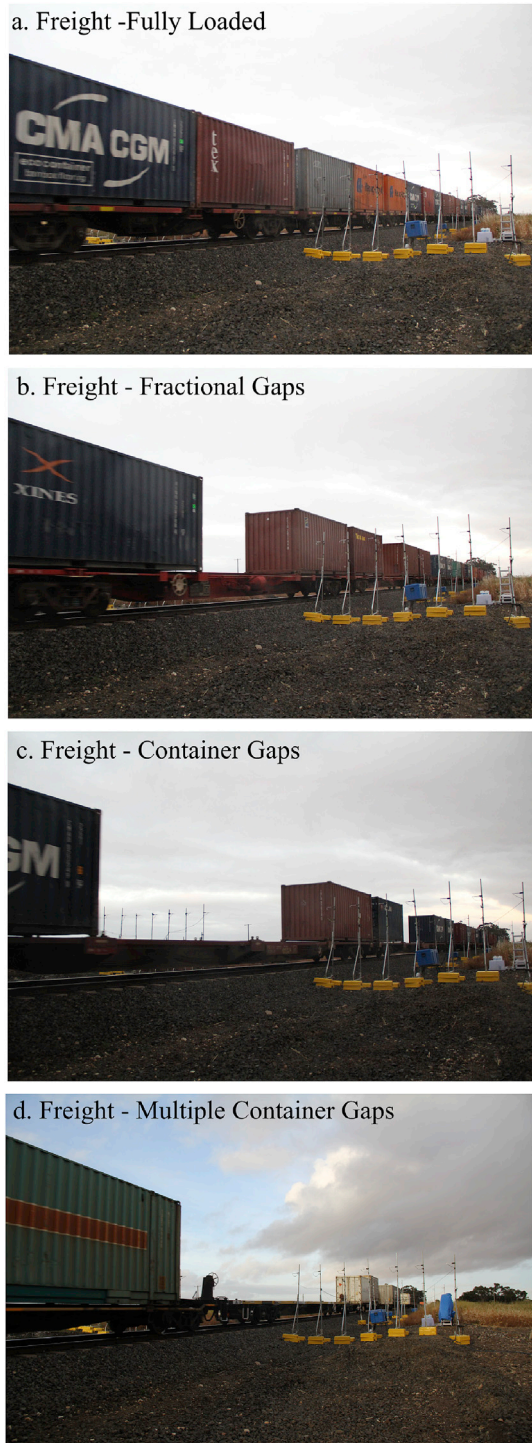


**Fig. 3.** Variety of gap sizes between shipping containers observed on the different operational freight trains.

travelling on a wagon on the rail. The subsequent probes were positioned at  $\Delta y = 1$  m increments in the horizontal direction. The probes were positioned  $z = 2.1$  m above the top of rail, which corresponds to approximately half the container height. This setup was consistent for all three rakes, where rakes R1 & R2 were positioned at the same distance along the track, on either side (Fig. 5 (a)) in order to provide insight into the correlation and coherence of the flow around the trains. Rake R4 was positioned on the same side as R1,  $\Delta x = 30$  m away.

Rake R3 contained 4 horizontal probes positioned in the manner described above, with 3 probes positioned in the vertical direction at

**Table 1**  
Test vehicles and test conditions.

Test Vehicles		Test Conditions			
No.	Gap Sizes	$u_t^1$ (m/s)	$u_a^1$ (m/s)	$\gamma$ (°)	$\beta$ (°)
T1	Small-Very Large	30.7	2.3	-4	-0.3
T2	Small-Medium	32.7	3.0	20	2.0
T3	Small-Large	31.1	4.0	12	1.8
T4	Small-Medium	29.9	4.4	149	3.9
T5	Medium-Very Large	24.5	5.0	-48	-9.9
T6	Small-Medium	26.1	7.0	-137	-8.7

$\Delta z = 0.5$  m increments, instead of the furthest 3 horizontal positions (Fig. 5(c)). These were positioned to gain insight into the vertical velocity gradient of the boundary layers.

Inside each equipment case were 32 channel Data Acquisition (DAQ) cards that were connected over the large distances to a laptop via Ethernet cables. Data was acquired at a sampling frequency of 1000 Hz, with sampling times of approximately 140 s. Power was supplied to the DAQ and measurement equipment by a battery. A laptop and the battery were charged using a portable generator; however, during actual measurement times they were disconnected from the generator and ran solely on battery power, to remove the possible effect of electrical noise caused by the generator.

The event of a train passing, and the position relative to the train nose were measured using two infra-red transmitter/receivers mounted on vertical supports of the 4-hole probes closest to the rail in rakes R1 and R3 (Fig. 5(d)). On the opposite side of the track was a reflective square element that reflected the transmitted infra-red light to the receiver (Fig. 5(e)). When the path (illustrated in Fig. 4(a) as red lines) was broken, a voltage change was measured in additional DAQ cards, thus each unit and reflector will be subsequently referred to as a ‘light gate’. The primary purpose of this equipment was to measure the train speed. However, these devices also provided insight into the loading configuration, as the light path was positioned at the height of the shipping containers, thus gaps between containers were recorded.

The ambient wind magnitude,  $u_a$ , and direction and temperature were measured at a 100Hz sampling rate by a weather station with an ultra-sonic anemometer. This was located on the vertical support of the probe furthest from the track in rake R1 (Fig. 5(a)).

### 2.3.1. Flow velocity

The velocity induced by the train’s movement was measured by 4-hole dynamic-pressure probes. These were designed, manufactured and calibrated by the Monash University Wind Tunnel Platform, and have previously been used – and the results published – in a scaled wind-tunnel experiment investigating the unsteady wake of high-speed trains (Bell et al. 2016a). The 100 mm long probes were positioned  $\Delta y = 200$  mm away from the primary vertical support and mounted in 14 mm diameter horizontal cylinders to reduce the interference the probe mounting could have on measurements. The mounting configuration of the probes is visible in Fig. 5(b).

The probes have a cone of acceptance of  $\pm 45^\circ$ , and therefore were rotated to face the direction of the oncoming train (facing opposite to the direction the trains were travelling) in order to measure the flow induced by the trains’ surfaces. The probes have an accuracy of approximately  $\pm 1$ m/s and  $\pm 1^\circ$ . Flow that was beyond the cone of acceptance ( $< 5\%$ ) was identified in processing through inspection of the pressure magnitude, sign, and pressure relative to the other holes on the probe. The pressure of each hole was measured with a differential pressure transducer referenced to atmospheric pressure. Atmospheric pressure was measured by a reference port connected to a plenum shielded in a container with small vents (to allow ambient pressure to exist within the container) located at each rake, within a protective equipment case that was also vented to the atmosphere.

Within each equipment case, located at each rake (see blue boxes in Fig. 4), was a 32 channel Dynamic Pressure Measurement System (DPMS).

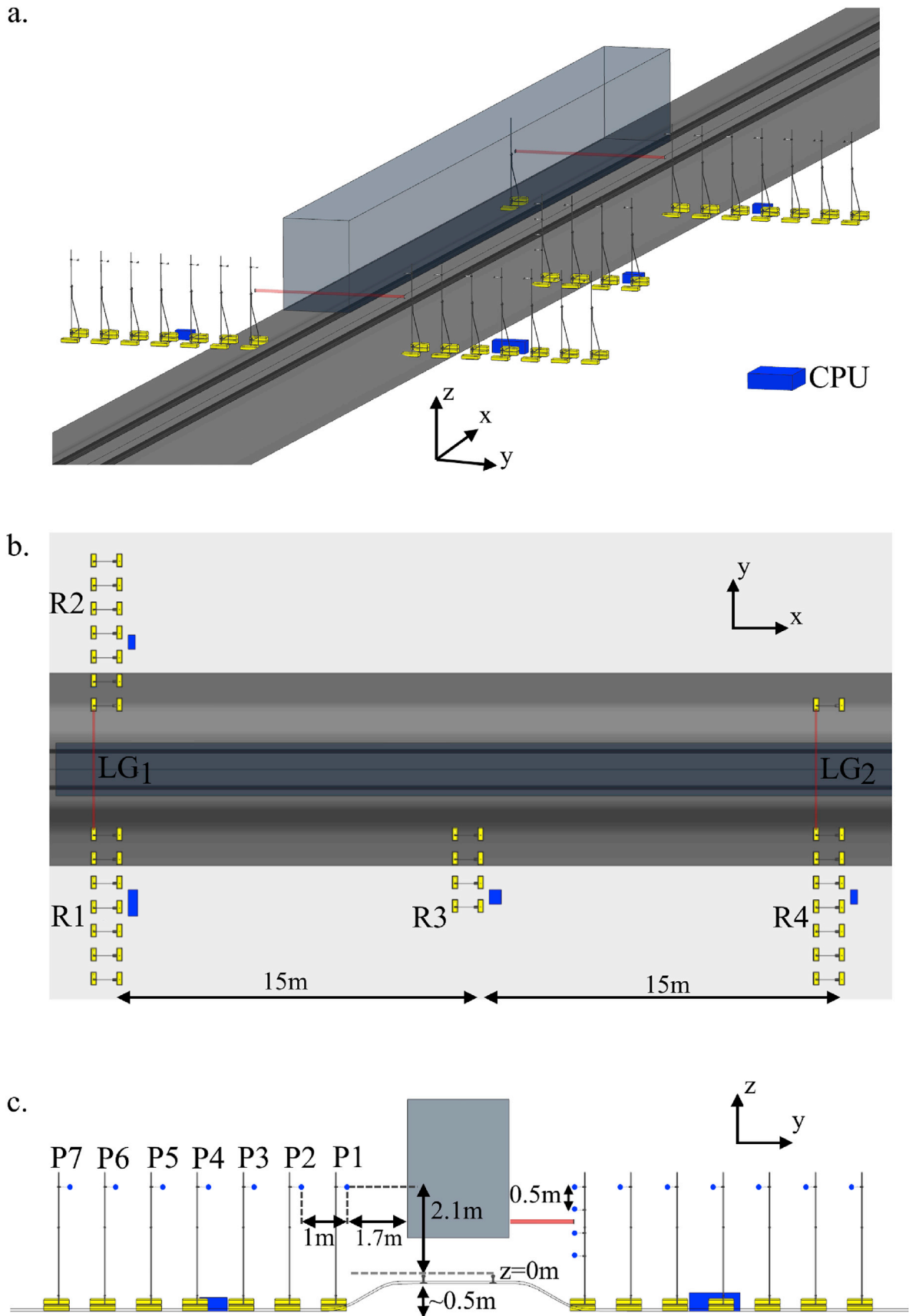


Fig. 4. Experimental setup: rakes (R1-R4) of 4-hole dynamic-pressure probes (P1-P7), light-gates (LG1-2) and light-beam paths (red), processing area (CPU) and data acquisition and measurement equipment boxes (blue) presented in (a). isometric, (b): top down, and (c): front-on perspectives. (For interpretation of the references to colour in this figure legend, the reader is referred to the Web version of this article.)

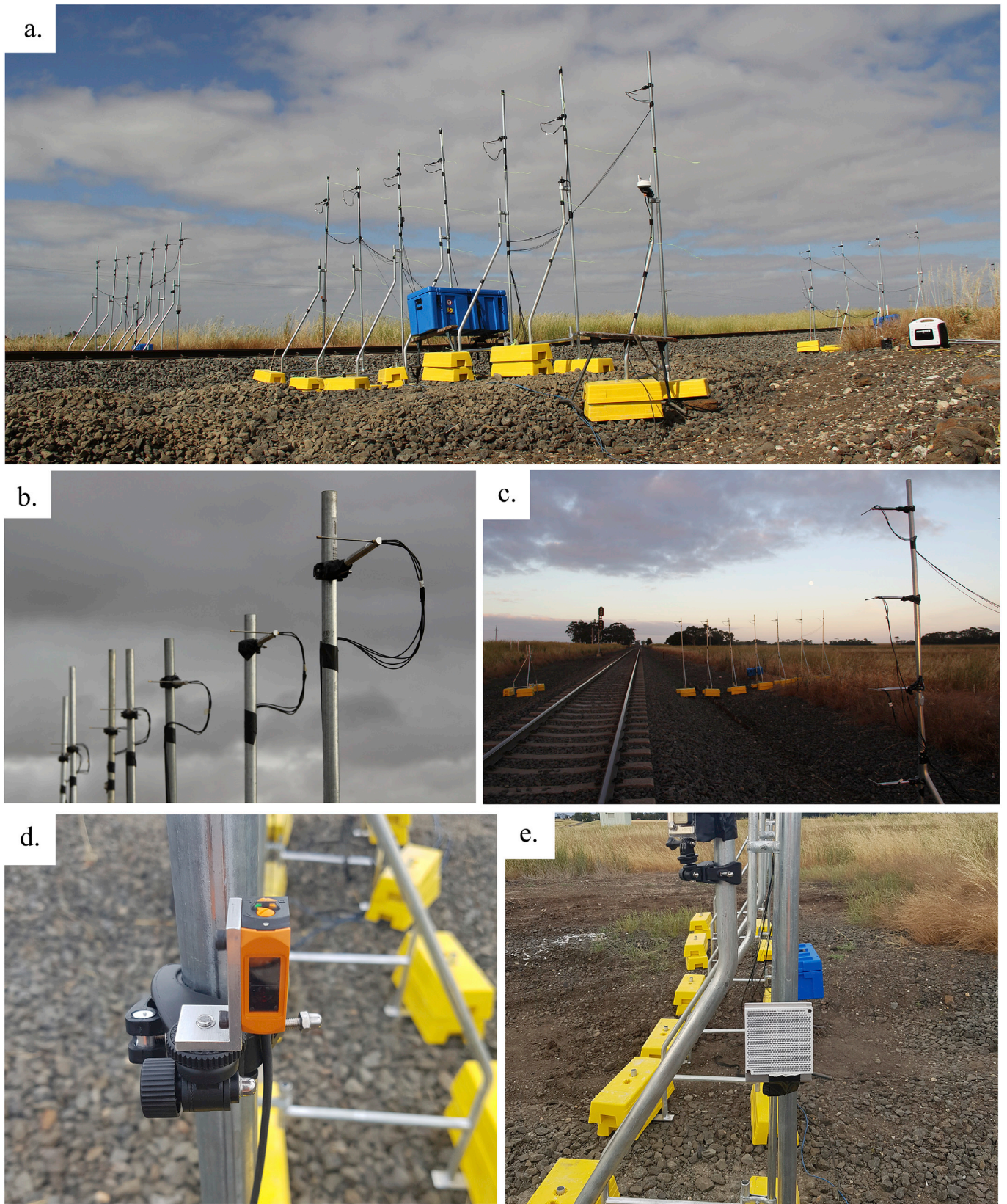


Fig. 5. Photos of the setup and experimental equipment. (a): rakes R1 and R2, probe support infrastructure and data acquisition boxes, (b): rake of probes, (c): vertical rake R3, (d): light-gate transmitter/receiver and (e): reflective element for light-gate.

Each hole of each probe was connected to a transducer in the DPMS by 4 m of 1.2 mm internal diameter Poly-Vinyl-Chloride (PVC) tubing.

The phase and amplitude of the pressure measured by the transducer is subject to distortion relative to the true pressure at the desired measurement point. This distortion occurs due to resonant characteristics of the system (Iberall, 1950). The amplitude and phase response for each measurement was corrected using the inverse transfer function (ITF) method (Irwin et al., 1979). The frequency response of the pressure measurement system was determined theoretically using a method outlined by Bergh and Tijdeman (1965). The system had no peak frequencies, and fell below an amplitude of 0.2 at 60 Hz. Beyond this frequency correction was not applied, in order to reduce the chance of noise amplification.

Dynamic-pressure probes were utilized instead of ultra-sonic anemometers - more commonly used in slipstream motivated investigations (Sterling et al., 2008) - initially due to cost and availability. More importantly, the use of a large number of probes resulted in a spatial resolution able to reasonably resolve the boundary layer, take simultaneous measurements either side of the track, and at different longitudinal locations - effectively measuring the passing of the same train 3 times.

### 2.3.2. Train velocity & position

As the two light gates were positioned 30 m from each other in rakes R1 and R4, the difference in time ( $\Delta t$ ) between the two light gates of the increase/decrease caused by the train's nose and tail passing in the output voltage signal was used to determine the train speed.

An example of the voltage signals of both light-gates is presented in Fig. 6(a). Here, the events of the step-up caused by the nose passing, and subsequent step-down as the tail moves past, are visible, as is light-gate 1 signal, clearly lagging light-gate 2 (the train was travelling West in this example). Fig. 6(b) shows the voltage of the pressure transducer from the probes closest to the track within each rake. Again, the lag of the head-pressure pulse is clearly visible due to the spatial offset of the probes location. The train velocity was calculated by

$$u_t = \frac{x_{LG_1} - x_{LG_2}}{t_{LG_1} - t_{LG_2}}, \quad (1)$$

where the longitudinal position of light gates  $LG_1$  and  $LG_2$ ,  $x_{LG_1, LG_2}$  were

set and thus known in the experimental setup, and the times when the train nose passes  $LG_1$  and  $LG_2$ ,  $t_{LG_1, LG_2}$ , were determined from the light-gate measurements.

The train velocity was calculated twice for each passage, using the nose and tail passing events separately. This enabled the acceleration to be calculated. In all cases, the train acceleration was minimal ( $a_t < 0.1 \text{ m/s}^2$ ), likely due the minimal separation distance between the light-gates relative to the scale of the train and track. As such the train speed  $u_t$  was simply taken as the speed calculated from the nose passing, without acceleration being considered. This train speed was used to convert the data from the temporal to the spatial domain. All data was then re-sampled to a common spatial resolution, and aligned relative to the train nose ( $x = 0$ ).

### 2.3.3. Flow visualisation

Additional insight into the induced flow field as the trains moved through the test site was achieved with high-visibility yellow wool-tufts. The wool tufts were fixed to the vertical support structures in rake R1, at each spanwise probe position and at multiple heights. It was expected they influenced by the support geometry to a degree. However, the tufts are able to indicate flow in all horizontal directions (they don't have a limited cone of acceptance angle as the pressure probes do), thus they provide complimentary qualitative results.

Photos of the wool tufts were obtained with a digital single-lens-reflex (DSLR) Canon 60D camera, with a focal length of 18 mm, f-stop of  $f/5.6$ , exposure time of  $1/500 \text{ s}$ , and frame rate of 4 Hz.

## 3. Results

The results of an individual train are presented first, to provide initial insight into the measurements obtained and the processing techniques applied. The boundary layer characteristics of all trains are then presented and compared, followed by the specification of a 'characteristic boundary layer', representative of an average train operating under minimal crosswind. Finally, insight into global and local flow features are presented through flow mapping, frequency and correlation analysis.

### 3.1. Velocity profiles

#### 3.1.1. Horizontal arrays

In this experiment, the flow induced by the train's movement is measured, thus induced velocity is highest, closest to the surface. The longitudinal velocity ( $u$ ) measured by each of the 7 probes in the horizontal rake, R1, for train T3, is shown in Fig. 7. These results are representative of the trains (T1, T2, T3) measured with low crosswind;  $u_a < 4 \text{ m/s}$  (relative yaw angle,  $\beta < 2^\circ$ ). The differences between the velocity measured at the different rakes (R1, R2, R4) are presented and discussed in the following sections. The velocity was filtered with a 1 s moving-average window for clarity.

The boundary layers around the freight trains are not simply two-dimensional, indeed, nor are they necessarily boundary layers in the purest sense. However, they are analysed here as 2D boundary layers here for simplicity, as previous researchers have done (Muld et al., 2013; Baker, 2010; Bell et al., 2015). Thus, the longitudinal velocity ( $u$ ) is of primary focus as it contributes most significantly to boundary layer flow (in this case also). The other velocity components are analysed in Section 3.3. Further, the flow is characterised in later sections with 2D boundary-layer parameters such as displacement thickness and shape factor. This enables a level of quantification of boundary layer thickness, and a method for comparison across different cases.

These results clearly show the existence and increasing thickness of the induced boundary layer along the length of the train. This is evident in the velocity being higher at positions close to the train (e.g.  $y = 1.71 \text{ m}$ ) than at positions further away from the train (e.g.  $y = 7.71 \text{ m}$ ). Furthermore, it can be seen that these induced velocities tend to increase along the length of the train. Significant fluctuations in velocity within

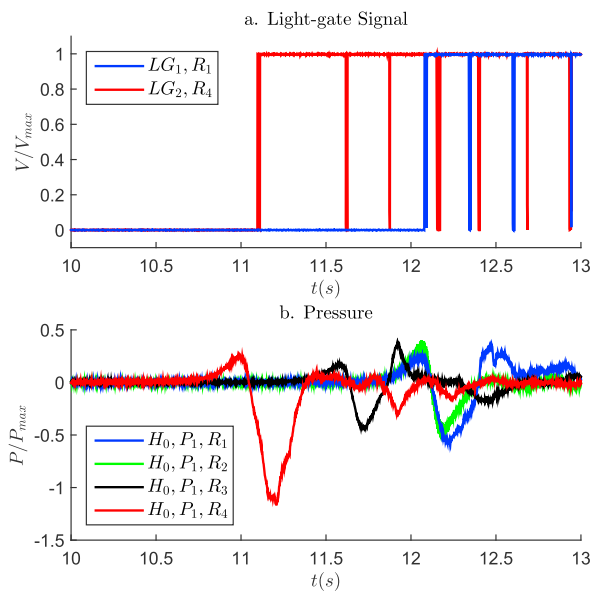


Fig. 6. (a): Normalised voltage signal from light-gates  $LG_1$  and  $LG_2$ . (b): Normalised pressure signals from the centre hole ( $H_0$ ) of each of the probes closest to the train ( $P_1$ ) within each rake ( $R_1$ - $R_4$ ).

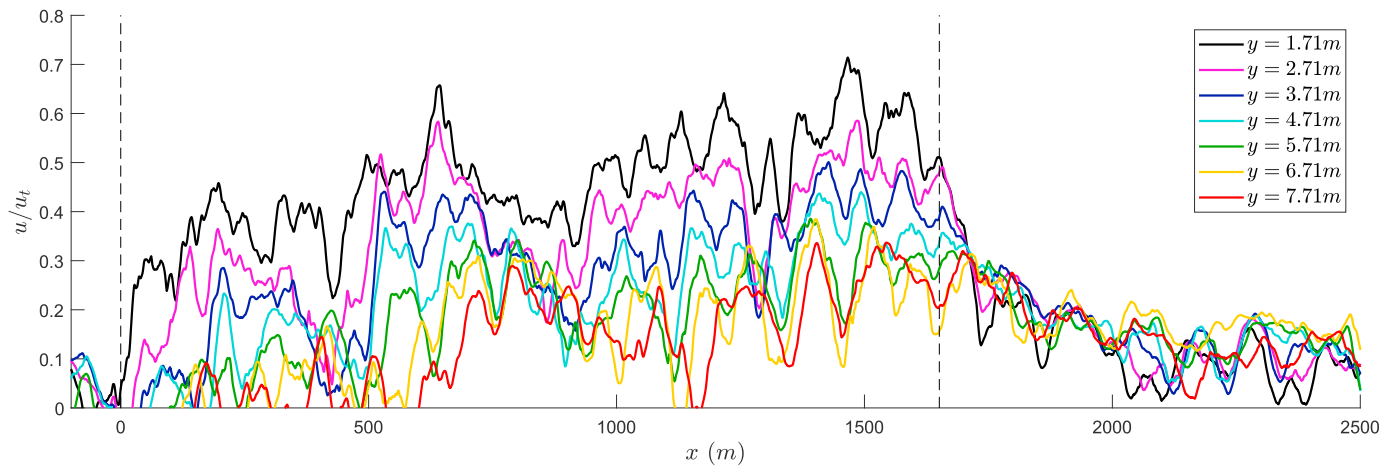


Fig. 7. Longitudinal induced velocity,  $u$ , normalised by train speed  $u_t$  measured by each probe in rake R1 for train T3. Dotted vertical lines indicate train nose and tail.

the boundary layer are largely consistent across the horizontal positions measured. In addition, a visible lag in the longitudinal direction exists for the probes further away from the train, caused by the flow disturbance requiring time to convect/diffuse to these positions.

These results are consistent with research into the slipstream of freight trains by Soper et al. (2014), Soper (2014), Sterling et al. (2008) which have also observed increasing induced velocity that reaches a maximum along the body – due to the boundary-layer thickness increasing – followed by the significant reduction of induced velocity after the tail. This is in contrast to the slipstream of high-speed trains which also exhibit increasing velocity along the length due to the boundary-layer thickness increasing, however, the highest velocities are found in the near-wake region (Bell et al., 2017; Sterling et al., 2008).

### 3.1.2. Vertical array

In contrast to the horizontal development of the boundary layer, trends in velocity profile in the vertical direction are not as clear. The longitudinal velocity ( $u$ ), measured by each of the 4 probes at a distance of  $y = 1.71$  m from the train, in the vertical rake, R3, again for train T3, are presented in Fig. 8. In general, at this position, the velocity is higher at the lower measured positions ( $z = 0.6$  m), closer to the ground, than the higher positions ( $z = 2.1$  m). This indicates that the boundary layer is thicker closer to the ground. Such a result is expected, and similar findings have been observed in the literature (Soper et al., 2014). This is proposed to be due to the presence of additional elements of the train

such as the wheels, bogies, and the coupling mechanisms of the wagons. Such elements are likely to increase the entrainment of the ambient flow. It is unclear how the ground plane affects the velocity closer to the ground and further away laterally from the train, as the lowest measurement was approximately 1.1 m above the local ground surface.

Interestingly, this trend of increasing velocity with increasing height is occasionally inverted, most notably at  $x = 750$  m in Fig. 8. At this point, velocity is highest away from the ground, and decreases towards it. There are clear signs of correlation in the velocity fluctuations between the vertically separated probes, but perhaps weaker than in the horizontal direction. Together with the inversion of the velocity gradient this indicates the existence of large-scale, three-dimensional, coherent structures within the boundary layer.

### 3.1.3. Horizontal boundary layer profiles

Boundary layer profiles at discrete positions along the train are presented in Fig. 9. These are developed from the same velocity measurements by each of the 7 probes in the horizontal rake, R1, for train T3. In this case, the results are presented simply to demonstrate the boundary layer velocity profile. Each sequential instantaneous discrete position was selected to illustrate the boundary layer growth along the train's length. Significant variation in these instantaneous profiles existed at different locations for the different trains, as can be expected from the transient velocity profiles in Fig. 7. The boundary layer profile at each spatial increment was developed, in order to calculate boundary layer

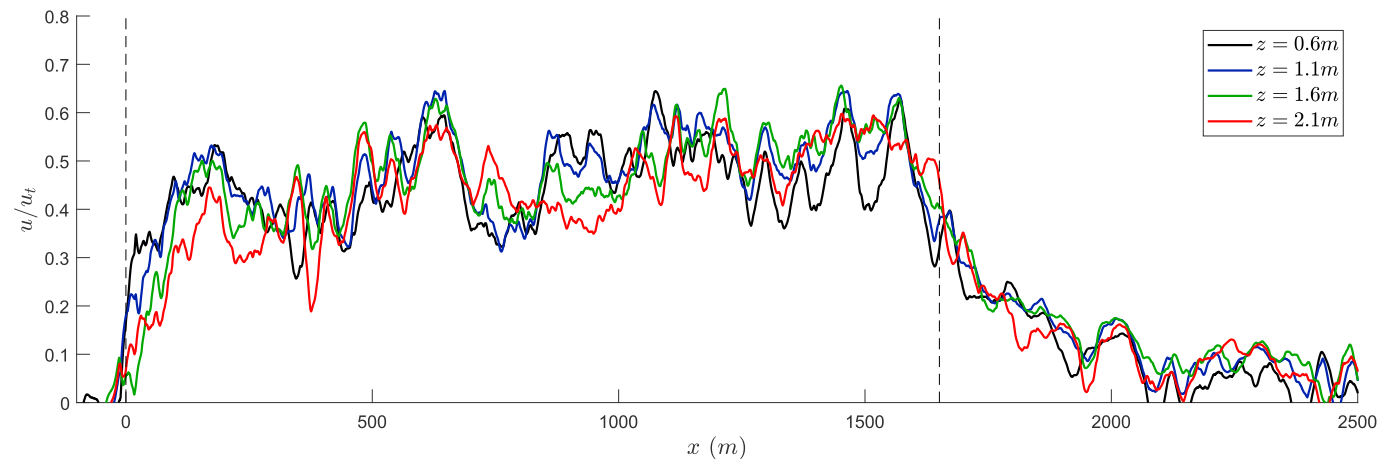


Fig. 8. Longitudinal induced velocity,  $u$ , normalised by train speed,  $u_t$ , measured by each probe in the vertical rake R3 for train T3. Dotted vertical lines indicate train nose and tail.

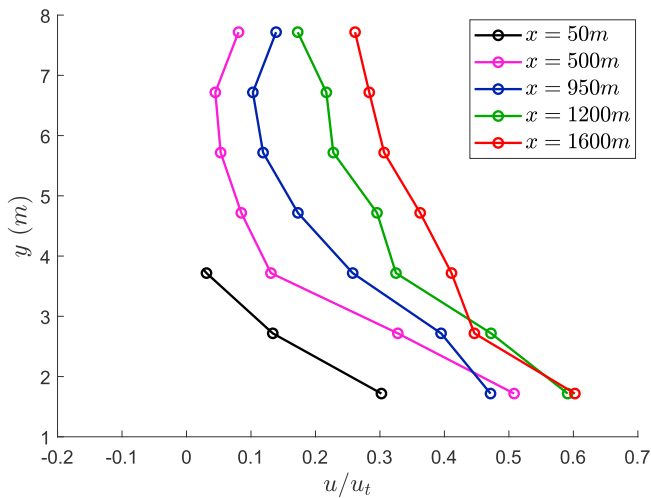


Fig. 9. Boundary layer velocity profiles determined from each of the 7 probes in rake R1 at different discrete longitudinal positions along the train.

characteristics along the train’s length. The corresponding characteristics are analysed and the differences between different rakes and trains are presented below.

### 3.2. Boundary-layer characteristics

The characteristics of the boundary layers for each of the 6 trains – low wind, and crosswind exposed trains – are presented and analysed in this section. Following this, a characteristic boundary layer is described, representative of a typical developed boundary layer around an inter-modal freight train. This is intended to help inform setting up experiments and numerical simulations intending to model real-world conditions.

#### 3.2.1. Displacement thickness & shape factor

Utilizing the boundary layer velocity profiles presented above, the displacement thickness was calculated using

$$\delta^*(x) = \int_0^\infty \left(1 - \frac{u}{u_t}\right) dy. \quad (2)$$

In Fig. 10, the displacement thickness for trains (T1, T2, T3) with low crosswind (relative yaw angle,  $\beta < 2^\circ$ ) are presented. Results from each individual rake (R1, R2, R4) are presented, as well as the ensemble average of all three.

For all three trains, the boundary layer thickness initially increases quickly up to  $\delta^* \approx 1$  m over the first  $\approx 200$  m. Following this, a further, slower development is evident up to a common range of  $\delta^* = 1\text{--}2$  m, within the full range of  $\delta^* = 0.5\text{--}3.5$  m. These values are higher than the range of  $\delta^* = 0.6\text{--}1.4$  m estimated by Soper (2014) in a 1:25 scale moving-model freight-train experiment and  $\delta^* \approx 0.1\text{--}0.3$  m measured by both Li et al. (2017) in a 1:14.6 scale freight-train wind-tunnel experiment and by Maleki et al. (2017) numerically. Further, these values are an order of magnitude higher than full-scale, operational high-speed train boundary layers estimated by Sterling et al. (2008) of  $\delta^* = 0.1\text{--}0.4$  m.

Relative differences between the measurements from the three rakes are also visible in Fig. 10. In particular, R1 and R4, positioned on the same side of the train exhibit very similar calculated displacement thickness, in contrast to that of R2, positioned on the other side of the train. A possible explanation for this, is the influence of the albeit minor crosswind, as the loading configuration is symmetric, and would be expected to influence both sides equally. It is for this reason that results from all three rakes are used to calculate the ensemble average. Even though it is likely that the measurements from rakes R1 and R2 are not independent from each other, as they are positioned at the same longitudinal position. The measurements from rake R2 were used in the calculation of averages, to include these differences to better represent the  $\hat{\alpha}\hat{\epsilon}$ -average  $\hat{\epsilon}^{\text{TM}}$  boundary layer of the trains measured.

The loading configuration of each train is expected to have an influence on the boundary layer that develops. In an attempt to quantify the loading configuration along the trains length – in order to compare directly the boundary layer displacement thickness – a cumulative blockage parameter was developed. This cumulative blockage at each spatial measurement increment,  $i$ , was calculated as

$$x_{B_i} = x_{B_{i-1}} + x_{\text{blocked},i}, \quad (3)$$

using the light-gate measurements, where  $x_{\text{blocked},i} = 1$  when the light-gate measured a path blocked by a container, or  $x_{\text{blocked},i} = -1$  when the light-gate path was not blocked, thus a gap existed. This parameter enables consecutive gaps, or conversely, containers packed closely together, to be visualised.

Profiles of cumulative blockage for trains T1, T2, T3 are presented in Fig. 11. Comparison of this parameter to the corresponding train displacement thickness in Fig. 10 shows that the relative changing cumulative blockage between the trains tends to match the relative displacement thickness; higher blockage (less gaps) approximately corresponds to a thicker boundary layer. Train T1 consistently has the lowest displacement thickness and cumulative blockage (the shallower gradient indicates it has small, consistent gaps) relative to trains T2 and T3.

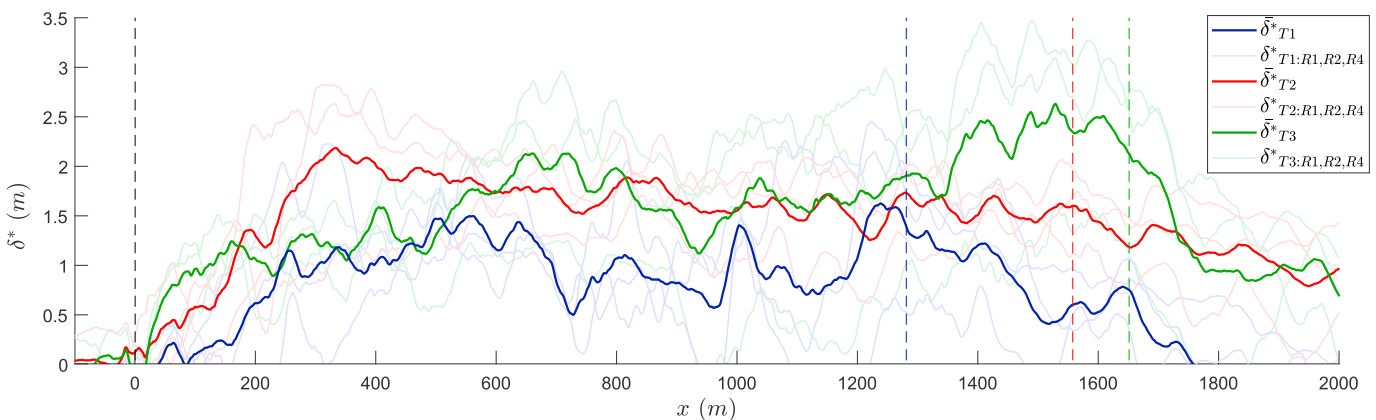


Fig. 10. Displacement thickness,  $\delta^*$ , profiles for each train (T1,T2,T3) with relatively low crosswinds ( $\beta < 2^\circ$ ). An ensemble average, as well as individual rake profiles are presented for each train. Dotted lines indicate the location of the train noses and respective tails.

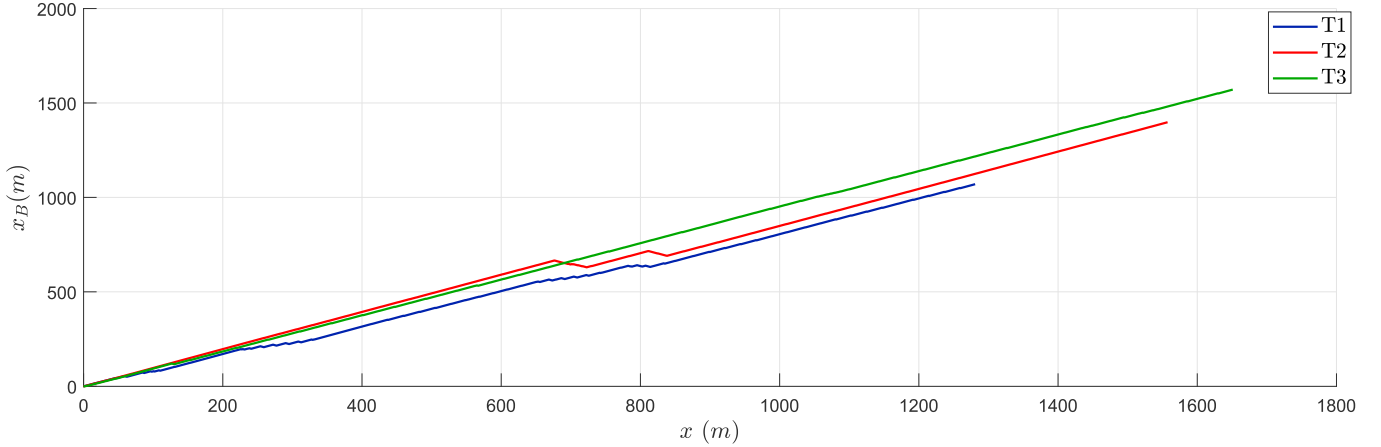


Fig. 11. Cumulative blockage profiles of trains T1, T2 & T3.

Further, T2 initially has a large displacement thickness and slightly larger cumulative blockage; however, from  $x \approx 600$  m, its blockage and displacement thickness both decrease, beyond which both remain lower than T3. Such results indicate loading configuration has an impact on the boundary layer, as one could expect; without the effect of crosswind, the boundary layer would be expected to increase along the length of the vehicle, sufficiently small gaps could have minor effect or act as ‘roughness’, while larger enough gaps would lead to separation of the flow that results in the boundary layer re-starting.

The shape factor is defined by

$$H(x) = \frac{\delta^*(x)}{\theta(x)}, \tag{4}$$

where

$$\theta(x) = \int_0^\infty \frac{u}{u_t} \left(1 - \frac{u}{u_t}\right) dy, \tag{5}$$

is the momentum thickness. This provides an indication of the form of the boundary layer profile. Profiles of the shape factor are presented in Fig. 12 for the three trains T1, T2, T3. No clear trends exist for the shape factor over the train lengths, indicating that the boundary layer form is relatively constant. The shape factor of  $H \approx 1.4$  indicates the boundary layer is turbulent, as expected.

The displacement thicknesses of the trains with higher crosswinds: T4 ( $\beta = 4^\circ$ ), T5 ( $\beta = 10^\circ$ ), T6 ( $\beta = -9^\circ$ ), are presented in Fig. 13. In this

case, the results from the different rakes R1 and R2 are designated as leeward, (LW), and windward (WW) relative to the crosswind direction.

Significant differences are immediately evident with the leeward and windward boundary layers. The crosswind essentially pushes the boundary layer towards the surface on the windward side, to the point where the probes are unable to measure a boundary layer. On the leeward side, the calculated displacement thickness is significantly larger than that observed for the trains with no/little crosswind:  $\delta_{LW:T4,T5,T6}^* = 2\text{--}4$  m, compared to  $\delta_{T1,T2,T3}^* = 1\text{--}2.5$  m, respectively. However, complex, three-dimensional flow is expected on the leeward side, not a simple structureless boundary layer, in which case the calculation of the displacement thickness is not entirely meaningful.

### 3.2.2. Turbulence characterisation

The flow that the measurement probes are exposed to as the trains pass is statistically non-stationary. Single events such as the nose/tail passing and unique gaps configurations, result in a flow that changes over time, rather than fluctuates around a consistent mean (a statistically stationary flow). Thus, the typical description of turbulence, quantified by turbulence intensity:

$$I_u = \frac{\sigma_u}{(u_t - \bar{u})}, \quad I_v = \frac{\sigma_v}{(u_t - \bar{u})}, \quad I_w = \frac{\sigma_w}{(u_t - \bar{u})}, \tag{6}$$

where  $\sigma_{u,v,w}$  and  $\bar{u}$  are calculated over an entire statistically stationary signal, is not applicable here.

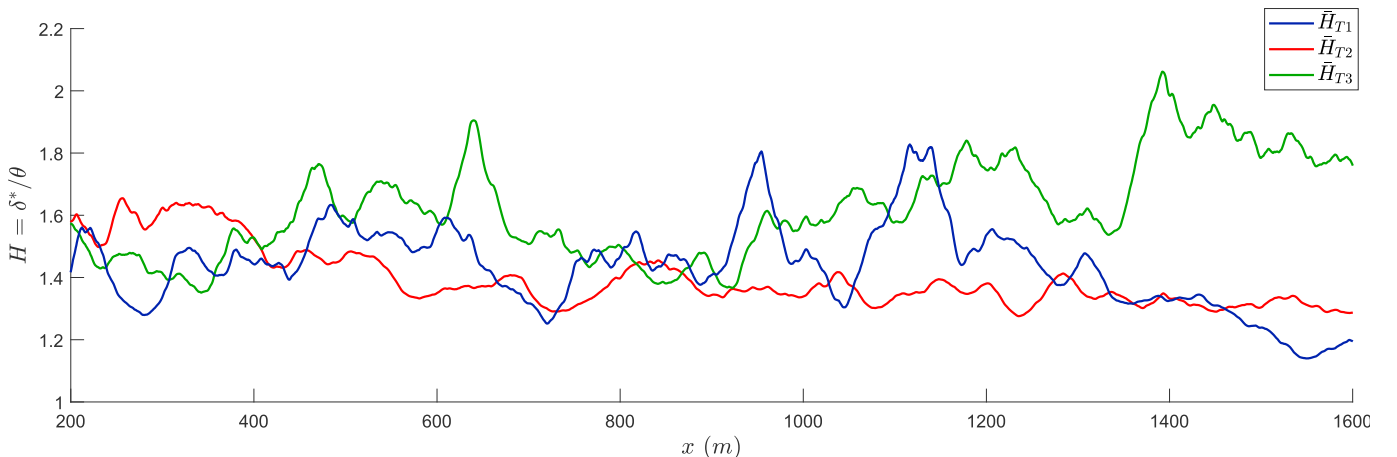


Fig. 12. Shape factor,  $H$ , profiles of trains T1, T2 & T3.

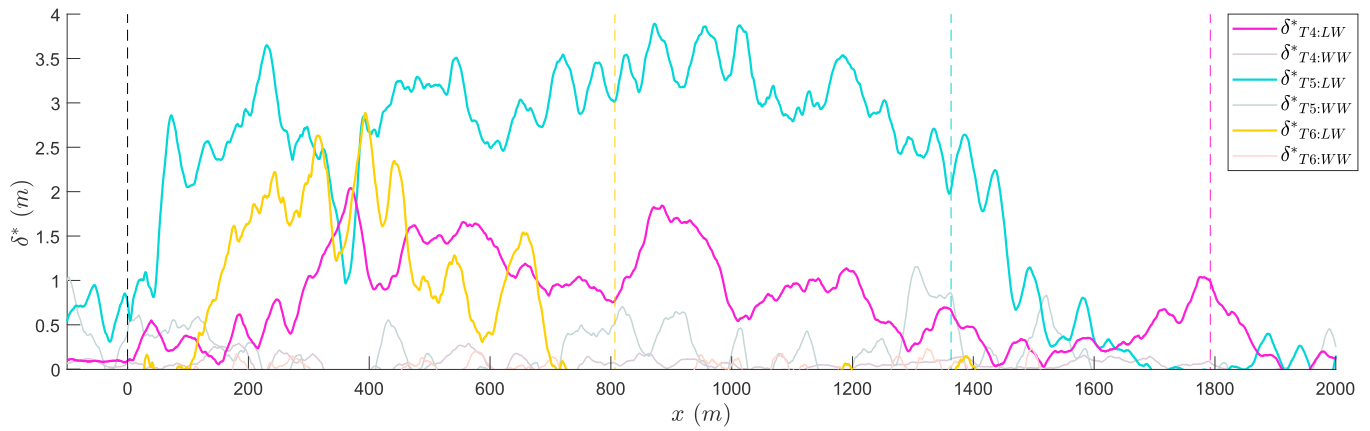


Fig. 13. Displacement thickness,  $\delta^*$ , profiles for each train (T4,T5,T6) with relatively high crosswinds ( $\beta > 2^\circ$ ). An ensemble average, as well as individual rake profiles are presented for each train. Dotted lines indicate the location of the train noses and respective tails.

In order to provide an indication of the turbulence within the boundary layer of full-scale freight trains, turbulence intensity along the train length is calculated over a moving window of filtered data. A single-pole Butterworth, 0.03–100 Hz band-pass filter was applied to the velocity measurements. The cut-off limits correspond respectively to a spatial length of less than the train lengths (0.03 Hz corresponds to  $\approx 1000$  m), and of the upper limit of the measurement system’s frequency response. In Fig. 14, the effect of the filtering of an example velocity time-series is illustrated, with the filtered result resembling a stationary signal. Regardless, a 5 s moving window was used to calculate the turbulence intensity over the length of the train:

$$I_u(x) = \frac{\sigma_u(x)}{(u_t - \bar{u}(x))}, \quad I_v(x) = \frac{\sigma_v(x)}{(u_t - \bar{u}(x))}, \quad I_w(x) = \frac{\sigma_w(x)}{(u_t - \bar{u}(x))}, \quad (7)$$

where  $\sigma_{u,v,w}(x)$  and  $\bar{u}(x)$  are calculated over a moving window equivalent to 5 s ( $x \approx 150m$ ) along the train length.

The longitudinal turbulence intensity,  $I_u(x)$ , calculated using equation (7), measured by each of the 7 probes in the horizontal rake, R1, for train T3, is shown in Fig. 15. These results are again representative of the trains [T1, T2, T3] measured with low crosswind;  $u_a < 4$  m/s (relative yaw angle,  $\beta < 2^\circ$ ). Turbulence intensities of 10–30% were measured, highest closest to the train, that increases along the length as the boundary layer thickness increases. These levels of turbulence are similar to the analogous case of on-road turbulence – what an automotive vehicle (of similar velocity and scale as shipping containers) experiences when

operating on the road, including the effect of the environment and other vehicles – characterised by Wordley and Saunders (2008) and McAuliffe et al. (2014) who found turbulence intensities of  $I_u = 2\text{--}16\%$ . In spite of the 5 s moving window over which the turbulence was calculated over, the profiles show significant fluctuation in turbulence along the length. This demonstrates specific loading configurations or local wind events (for example at  $x = 800$  m), can have a significant impact on the boundary layer characteristics beyond the velocity profile.

In Fig. 16, the different components of turbulence intensity,  $I_u, I_v, I_w$ , are presented for probe P1, in rake R1, for train T3. The anisotropic characteristics of the turbulence are relatively consistent:  $I_u : I_v : I_w \approx 1 : 0.4 : 0.6$ , as the turbulence generally increases, with additional fluctuations along the train length. Interestingly, greater turbulence exists in the vertical direction than the horizontal. This is contrary to that generally found on roads by Wordley and Saunders (2008), who determined anisotropic ratios of  $I_u : I_v : I_w \approx 1 : 1 : 0.6$ , where the proximity to the ground is expected to reduce the level of velocity fluctuations. A potential explanation for this difference is that in these experiments, measurements were made specifically next to the vehicle, in contrast to general exposure to the effects of a number of vehicles and infrastructure characterised on-road.

The turbulence intensities,  $I_u$  and  $I_{u,v,w}$ , calculated using equation (6) over the middle 40% of the train, are presented on the vertical axis as points in their respective colours for all probes in Fig. 16. This shows the different components of the closest probe in Fig. 15, respectively. The

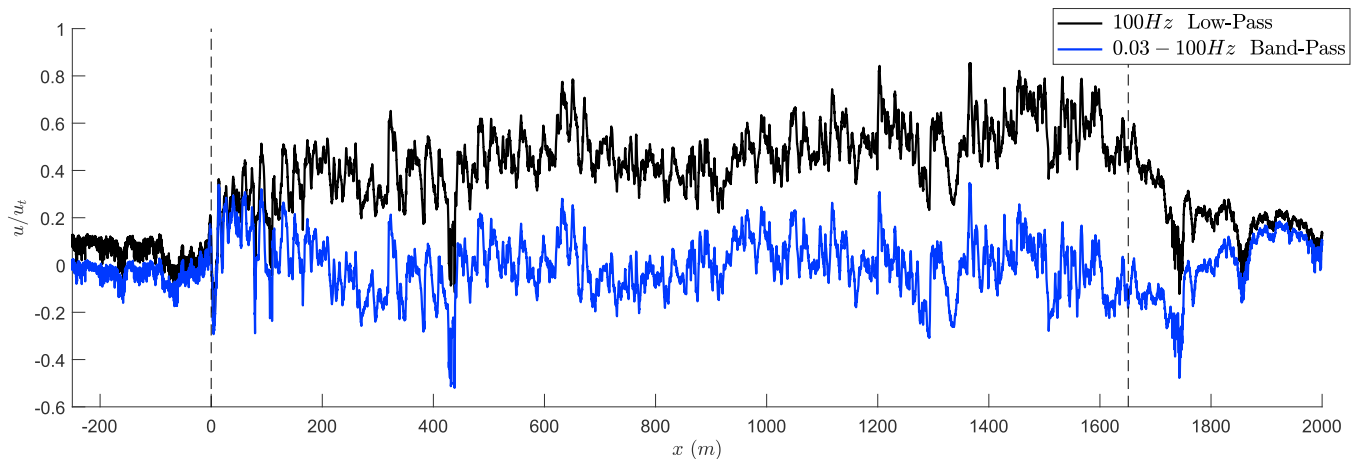


Fig. 14. Normalised longitudinal velocity of P1, T1 with a 100 Hz low-pass and 0.03–100 Hz band-pass single-pole Butterworth filter applied, used to calculate turbulence intensity.

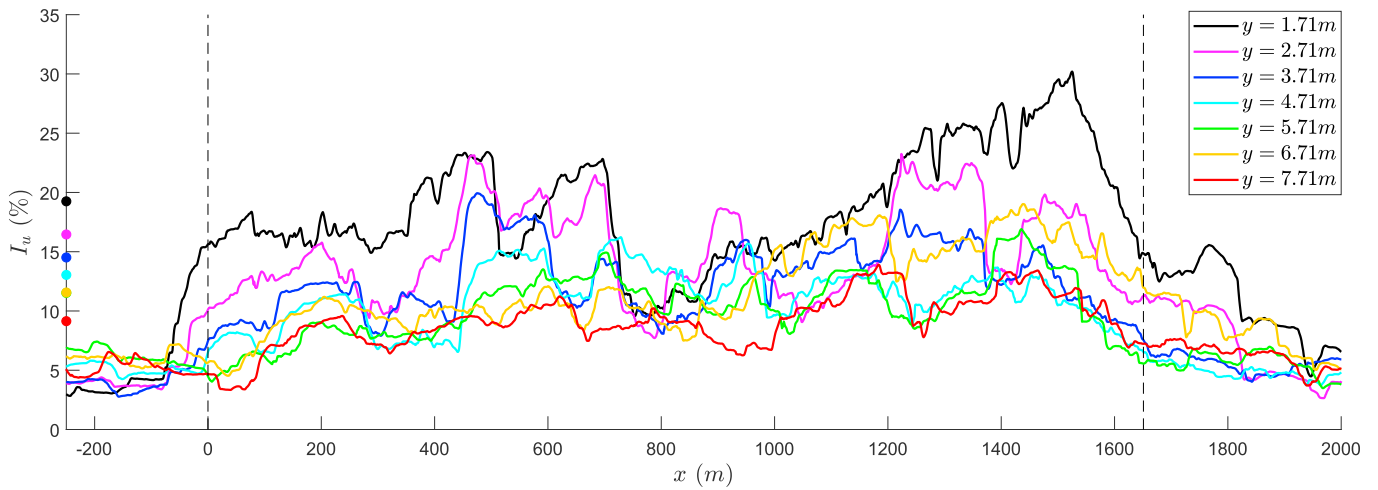


Fig. 15. Longitudinal turbulence intensity  $I_u$  profile along the train T3, calculated over a 5 s moving window at each probe in rake R1. Average of the middle 40% of the train presented as corresponding coloured points on the vertical axis.

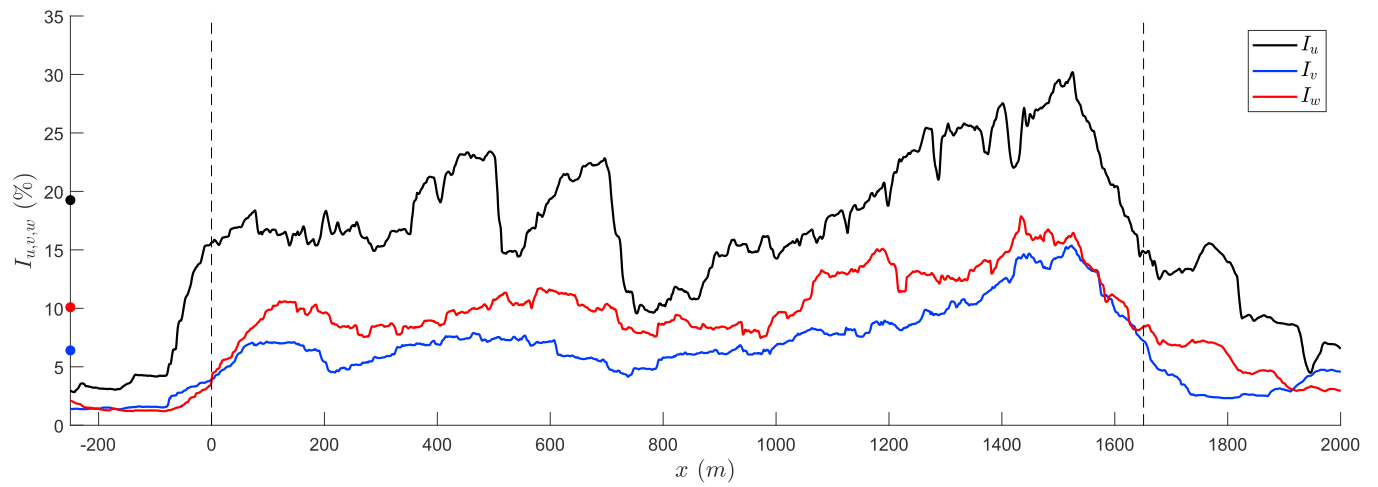


Fig. 16. Profiles of the different components of turbulence intensity  $I_u, I_v, I_w$  along train T3, at probe P1, in rake R1. Average of the middle 40% of the train presented as corresponding coloured points on the vertical axis.

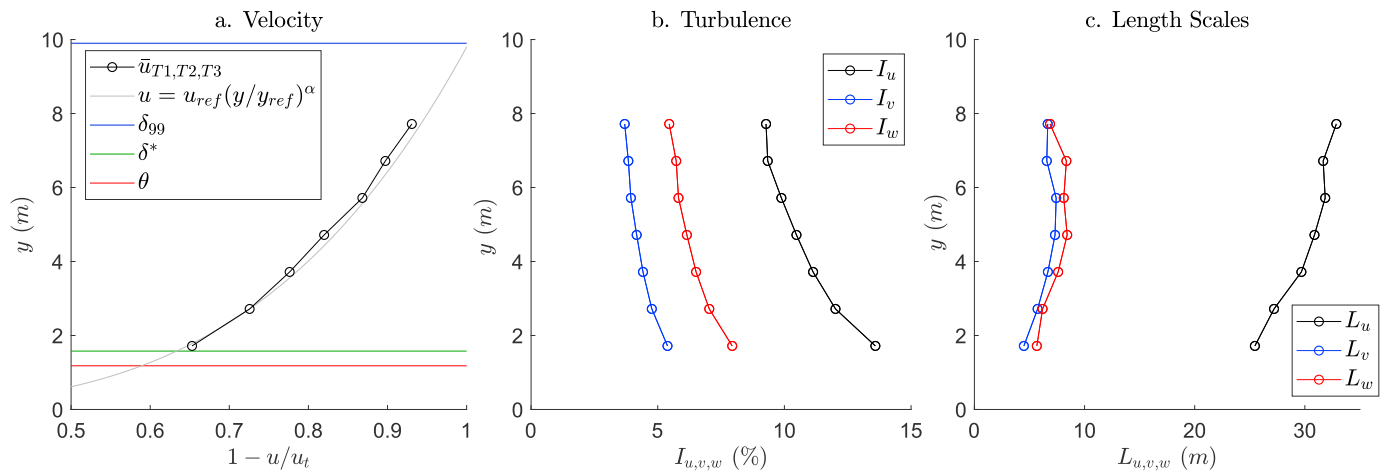


Fig. 17. Characteristic boundary-layer properties: (a) Velocity (mean velocity, estimated boundary layer thickness, displacement thickness and momentum thickness), (b) turbulence, and (c) length-scale profiles.

middle 40% was calculated as the section of train where  $x = 0.3L_t : 0.7L_t$ , where  $L_t$  is the length of each train and was selected to exclude the effect of the nose and tail flow regions, to best represent a representative, if somewhat arbitrary, middle section of a freight train.

### 3.2.3. Characteristic boundary layer

The boundary-layer characteristics measured by all three horizontal rakes (R1, R2, R3) for the middle 40% section of the three trains measured with low crosswind (T1, T2, T3) ( $u_t < 4$  m/s, relative yaw angle  $\beta < 2^\circ$ ) have been averaged and are presented graphically in Fig. 17 and tabulated in Table 2. These results are intended to be a reference for future investigations intending to model (or compare to) realistic boundary-layer characteristics experienced by an intermodel freight train. The corresponding standard deviation of each of the average characteristics are also presented at the bottom of Table 2 to provide an indication of the variability from the different rakes and trains measured.

The velocity, turbulence intensity and length-scale profiles of the characteristic boundary-layer are presented in Fig. 17(a), (b) and (c), respectively. Included in Fig. 17(a), are the displacement thickness ( $\delta^*$ ) and momentum thickness ( $\theta$ ), based on the calculated average velocity profile. The boundary layer thickness ( $\delta_{99}$ ) was estimated from where  $u \approx 99\%$  of the ‘freestream’ velocity, from a simple power-law model of the velocity profile:

$$u = u_{ref} \left( \frac{y}{y_{ref}} \right)^\alpha \tag{8}$$

where  $\alpha = 0.25$  and  $u_{ref}$  was the measured velocity at  $y_{ref} = 1.71$  m. These values are also provided in Table 3.

The anisotropic characteristics of the turbulence identified above for train T3, are the same in this characteristic boundary layer;  $I_u : I_v : I_w \approx 1 : 0.4 : 0.6$ , and remain consistent across the boundary layer thickness.

The length scales presented in Fig. 17(c) were estimated by least-squares fitting of the Kármán spectra to the velocity measurements with the same single-pole Butterworth, 0.03–100 Hz band-pass filter described above, for the middle 40% section of each train. These results are again similar to on-road turbulence length scales of  $L_{u,v,w} = 2\text{--}10$  m (Wordley and Saunders, 2008; McAuliffe et al., 2014).

### 3.3. Flow topology

The flow topologies around each of the freight trains are presented in two-dimensional planes in this section, complimented by wool-tuft flow visualisations. The three components of velocity,  $u, v, w$ , measured simultaneously by each probe using rakes R1 and R2, and for all trains, are presented in Figs. 18–20, respectively. Note that in these and subsequent 2D spatial figures, the  $x$  and  $y$  axes are not presented with a true 1:1 scaling, in order to more easily interpret the data. These results enable further insight into the cause of the development and significant fluctuations in boundary-layer thickness along the length of the trains, and difference between each side of each train.

**Table 2**  
Characteristic boundary-layer properties for the low crosswind cases (T1, T2, T3).

$y$ (m)	$1 - u/u_t$	$I_u$ (%)	$I_v$ (%)	$I_w$ (%)	$L_u$ (m)	$L_v$ (m)	$L_w$ (m)
1.71	0.65	13.6	5.4	7.9	25.4	4.5	5.7
2.71	0.72	12.0	4.8	7.0	27.2	5.7	6.2
3.71	0.77	11.1	4.4	6.5	29.7	6.7	7.6
4.71	0.81	10.5	4.1	6.1	30.9	7.3	8.4
5.71	0.87	9.9	3.9	5.8	31.8	7.4	8.1
6.71	0.89	9.3	3.9	5.7	31.7	6.6	8.4
7.71	0.93	9.3	3.7	5.5	32.8	6.6	6.9
$\sigma$	0.08	1.7	0.5	0.8	9.5	2.4	2.4

**Table 3**  
Boundary layer thickness characteristics for the low crosswind cases (T1, T2, T3).

$\delta_{99}$ (m)	$\delta^*$ (m)	$\theta$ (m)	$H$
9.9	1.6	1.2	1.34

#### 3.3.1. Global topology

Clearly visible in Fig. 18 is the significant difference in the  $u$  velocity for the trains with low crosswind (T1, T2, T3) to the trains experiencing higher crosswinds (T4, T5, T6). Even for the trains under low crosswind, the flow around the train is asymmetric, which is unlikely to be caused by the predominantly symmetric loading configurations. This is clearer for T2 and T3, where a thicker region of induced flow on the positive  $y$  side of the trains – consistent with the positive  $\beta \approx 2^\circ$  ambient wind for both trains. Here, the (albeit low-level) crosswind effectively pushes the boundary layer towards the train surface, reducing its thickness on the windward side and increasing the level of induced flow on the leeward side to a peak of  $0.6u_t$ . This is seen to a significantly greater extent for the high crosswind trains (T4, T5, T6), where the boundary layer is reduced beyond the measurement points on the windward side, and the induced velocities increase to a level of up to  $0.8u_t$  on the leeward side.

Regardless of the observable influence of the low-cross wind on the flow topology, trains T2 and T3 also show the growing of the boundary layer along the train length. In contrast, train T1 exhibits fluctuations between stages of development and significant reduction, with considerably greater symmetric flow. These trends are also visible in the boundary layer displacement thickness profiles in Fig. 10, with T2 and T3 developing to a larger displacement thickness. As noted in Table 1, and quantified in Fig. 11, the loading configuration of T1 contained the larger and more consistent gaps. Therefore, the loading configuration can be attributed as the cause for reduced boundary layer size. The greater symmetry observable for T1 is likely attributable to the lower crosswind ( $\beta = -0.3$ ). However, the smaller boundary layer caused by the loading configuration may also result in the flow field being less sensitive to crosswind that is less observable in these results.

Inspection of the horizontal velocity component,  $v$ , in Fig. 19 identifies the initial flow away from the head of the train ( $x = 0m$ ). The flow then generally tends towards the train surface with a magnitude of  $v \approx 0.08u_t$ , with relatively incoherent oscillations along the trains. Stronger horizontal flow ( $v \approx 0.1u_t$ ) towards the rail centre occurs after the tail has passed as the wake closes. This is most clearly visible for train T2 in Fig. 19(b), and highlighted specifically with  $u, v$  velocity vectors presented in Fig. 23.

#### 3.3.2. Local topology

An apparent correlation is evident between the fluctuations in  $u$  and  $v$  velocity beyond the effect of crosswind already described. This occurs most clearly at  $x = 400$  m and  $x = 800$  m for train T1, where on the positive  $y$  side of the train, a large region of flow with an increase in  $v$  velocity directed towards the train, corresponds to a decrease in  $u$  velocity. The  $u$  velocity in the region over  $x = 400\text{--}800$  m is presented in Fig. 21 and  $u, v$  vectors over  $x = 600\text{--}700$  m in Fig. 22, with the loading configuration also illustrated from the light-gate measurements. In Figs. 21 and 23, the turbulent flow field is visualised, with some indications of vortex structures existing in the flow arising from the shear layer interaction between the high velocity induced flow near the train surface and the ambient wind away from the train. However, from these results, a single gap on its own does not have a singular identifiable effect on the flow. It appears that it is the cumulative combination of a series of gaps that results in flow that is analogous to that seen at the tail of the train (Fig. 23) and the overall decrease in the bulk induced flow.

The vertical velocity component,  $w$ , presented in Fig. 20 shows regions of fluctuating sign at much smaller scales ( $\approx 10\text{--}25$  m) than the fluctuations in longitudinal,  $u$  velocity ( $> 100$  m). This is evident most clearly for train T3, but also for trains T1, T2 and T4 on the leeward side.

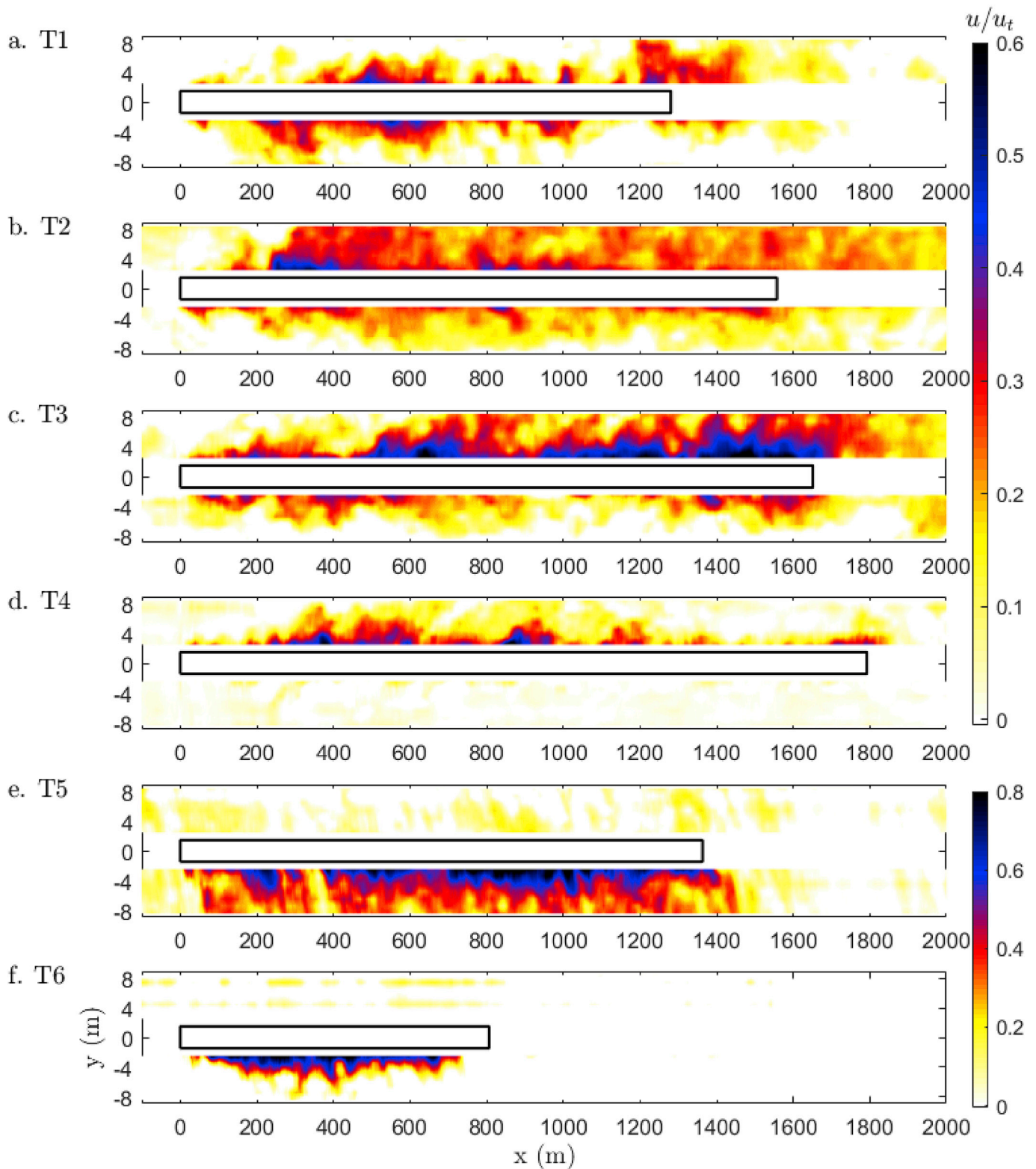


Fig. 18. Coloured contours of longitudinal velocity,  $u/u_t$ , around trains T1–T6: (a)–(f). The position of each train indicated by a black outlined box.

These fluctuations are strongest ( $w = \pm 0.1u_t$ ) closest to the surface, and convect away, lagging behind the point of origin. A possible explanation for such vertical velocity fluctuations and approximate length scales is the formation of horseshoe-type vortices rolling up in front of individual shipping containers with enough of a gap at the front to experience relatively clean flow. Although interesting, these result do not appear to have a significant effect on the overall boundary layer development.

The horizontal,  $v$  (Fig. 19), and vertical,  $w$  (Fig. 20), velocity components are difficult to interpret for the trains with high-crosswind (T4,T5,T6). The leeward side is expected to exhibit a three-dimensional flow topology, primarily consisting of a semi-longitudinal vortex that develops from separation at the leeward upper edge (Hemida and Baker, 2010; Copley, 1987). The  $v$  and  $w$  velocity magnitude and direction measured by the probes in the horizontal array are therefore dependent

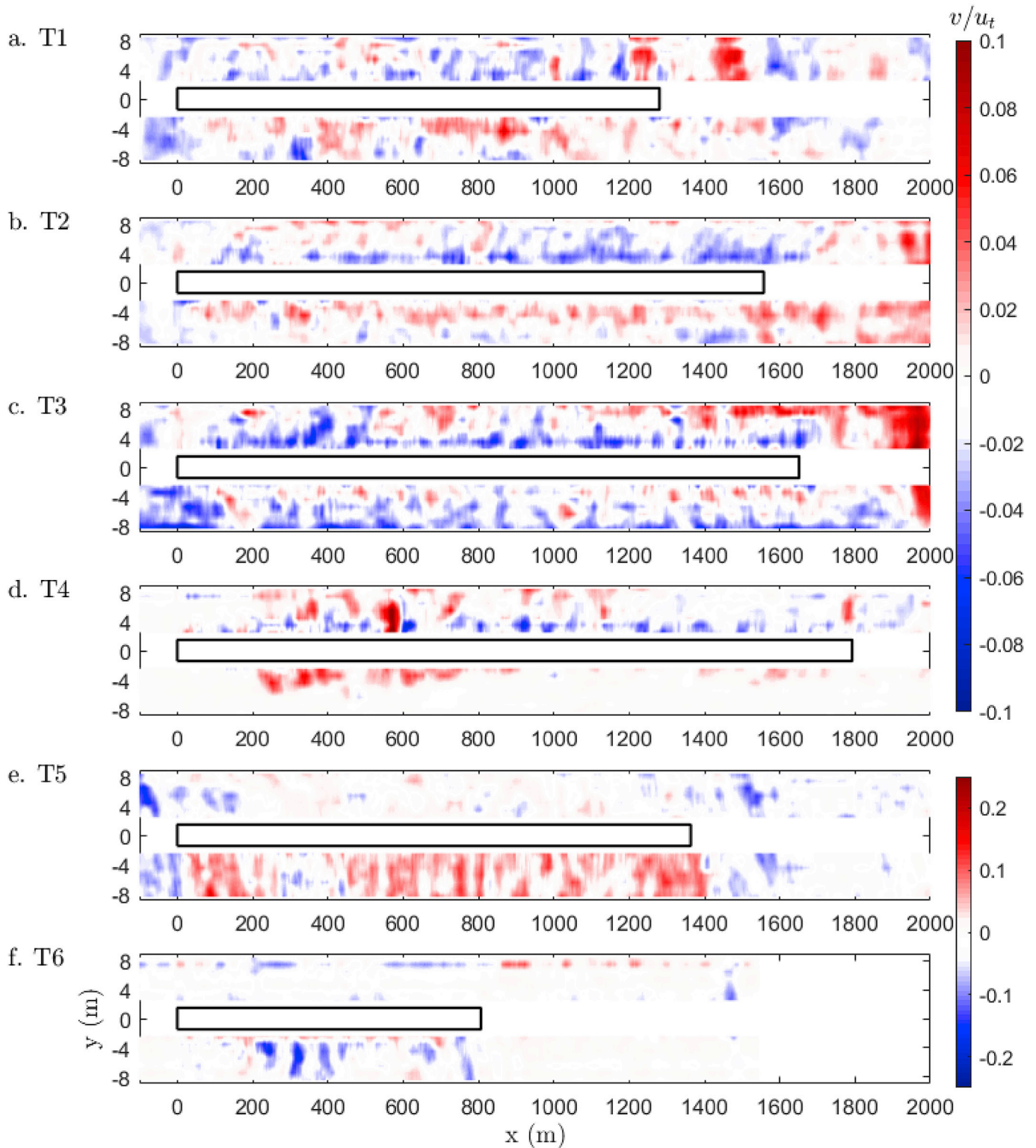


Fig. 19. Coloured contours of horizontal velocity,  $v/u_t$ , around trains T1–T6: (a)–(f). The position of each train indicated by a black outlined box.

on the relative height of the structure as it passes through the array. In addition, such a structure is likely unsteady itself, and further influenced by the unsteady crosswind and non-uniform loading configuration. Thus, the  $v$  and  $w$  velocity figures are inconsistent for the different trains with high crosswinds, and no clear trends or characteristic features are able to be determined.

### 3.4. Frequency analysis

Frequency analysis was performed on the velocity measurements. In Fig. 24, the frequency spectra from the seven probes in rake R1 calculated over the middle 40% of train T1 are presented for the different velocity components. The power spectral density was estimated using the Welch

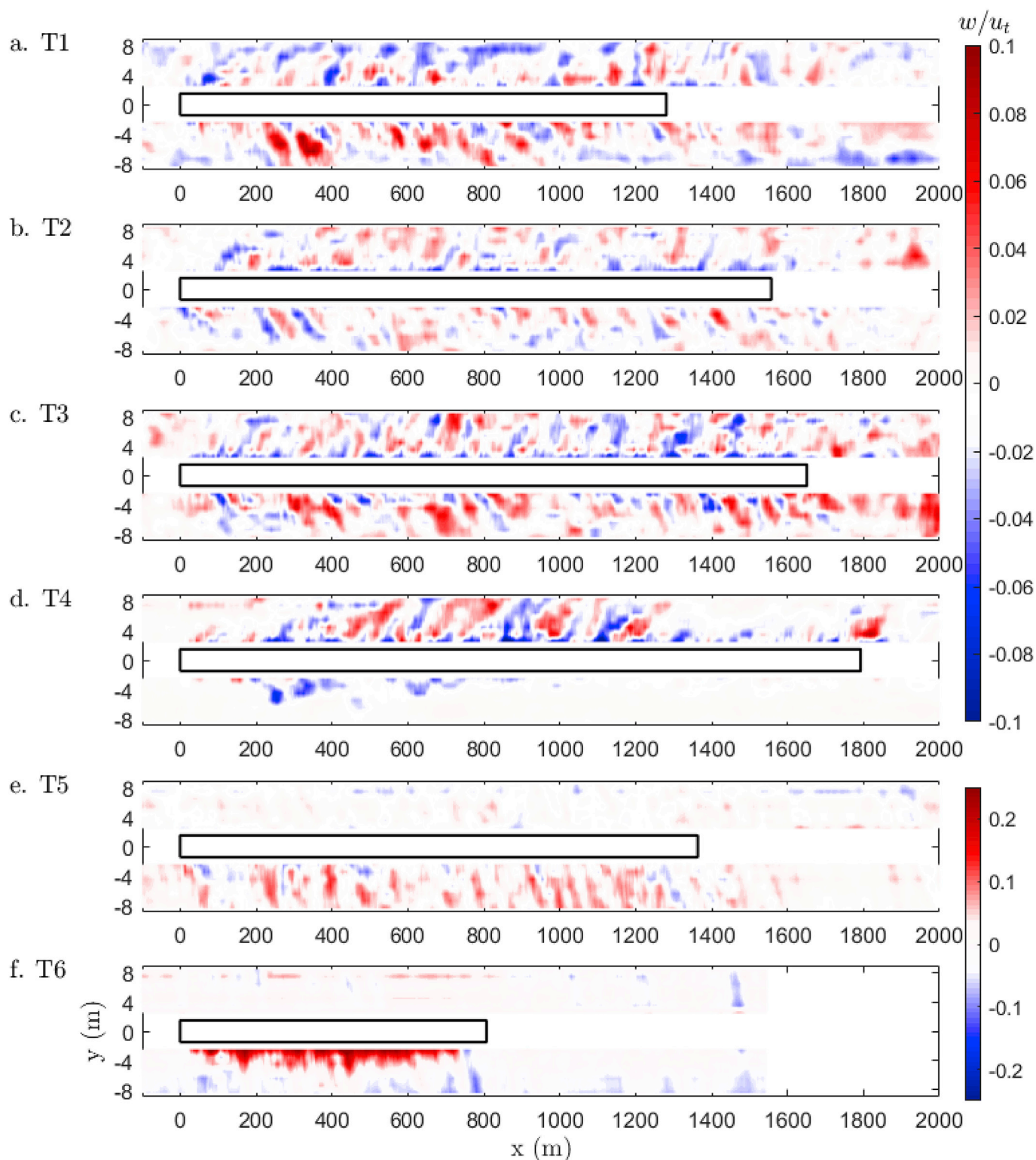


Fig. 20. Coloured contours of vertical velocity,  $w/u_t$ , around trains T1–T6: (a)–(f). The position of each train indicated by a black outlined box.

method with 8 Hamming windows and 50% overlap. The results are representative of the low crosswind trains (T1, T2, T3).

A broad frequency band over the range of  $f = 0.5\text{--}5$  Hz with various specific peaks at  $f \approx 1, 1.5, 2$  and  $3$  Hz are visible for all three velocity components. This band becomes stronger, closer to the train. Additional higher frequency peaks at  $f \approx 22$  Hz and  $f \approx 35$  Hz are also visible in the spectra across all of the measurement positions.

Due to the relative motion between the vehicle, the surrounding

induced fluid flow and the measurement probe, it is difficult to separate periodic aerodynamic features (e.g. vortex shedding, as observed by Li et al. (2017) in the wake of containers) and periodic features caused by the train moving past the measurement equipment (e.g. repetitive passing of individual containers, ribs on the containers, wagons and bogies).

Vortex shedding from the sides of containers, if existent, would correspond to  $f \approx 3$  Hz (from an approximate Strouhal number of  $St_w \approx 0.2$  based on the container width). Higher frequency shear-layer vortices

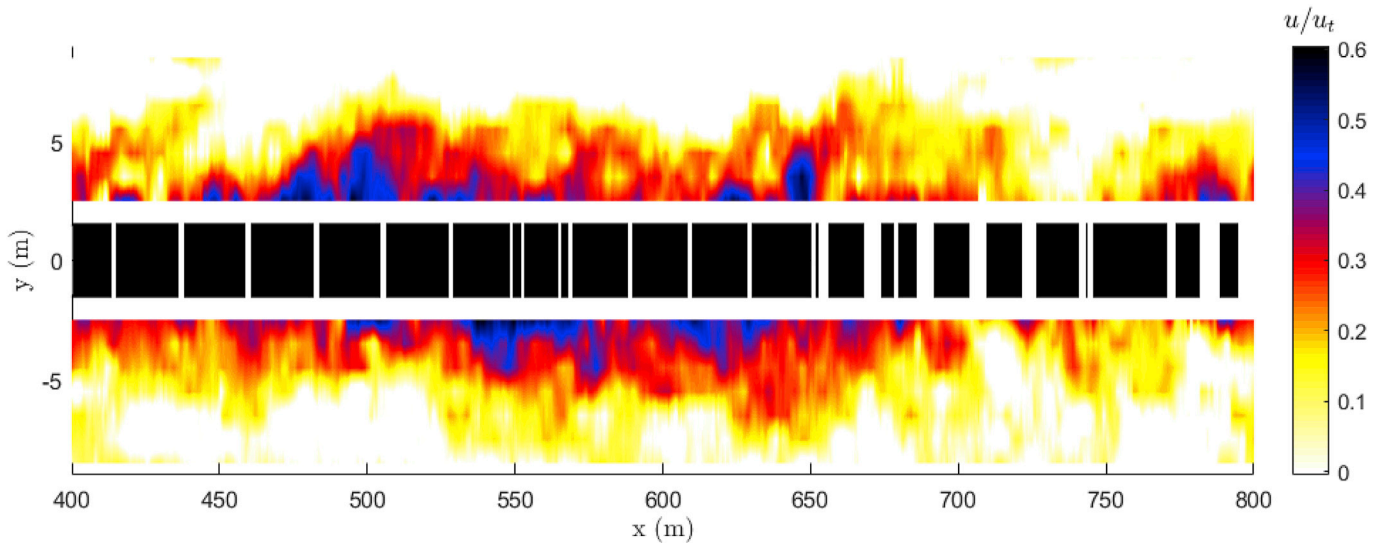


Fig. 21. Coloured contours of longitudinal velocity,  $u/u_t$ , around train T1 over the section  $x = 400\text{--}800$  m with a series of consecutive gaps. Train indicated by black box and gaps by white spaces.

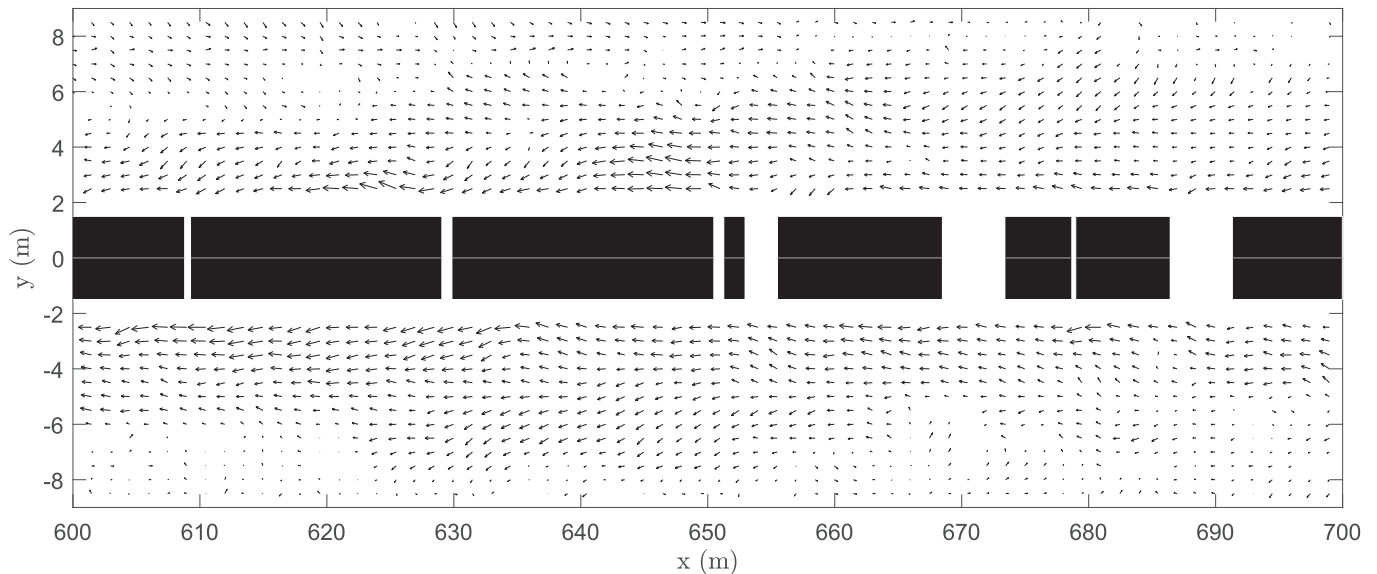


Fig. 22. Velocity vectors of  $u, v$ , around train T1 over the section  $x = 600\text{--}700$  m with a series of consecutive gaps. Train indicated by black box and gaps by white spaces.

could also occur with  $f \approx 23$  Hz ( $St_w \approx 1.5$ ). Conversely, repetitive signals observed in the light gate measurements with length scales of 17–22 m associated to the wagons and/or containers passing the measurement position, correspond to frequencies of  $f \approx 1.4\text{--}1.75$  Hz. Repetitive signals from the container ribs ( $x \approx 0.2$  m) correspond to much higher frequencies of  $f \approx 150$  Hz. These values are based on the train speed of  $u_t = 30$  m/s. However, the boundary layer is also likely to modify the flow conditions such estimations are based on. This could result in a reduced effective velocity, and increased effective widths, and therefore different corresponding expected frequencies.

Although minor trends and features in the spectra can be observed, there are no clear dominant frequencies that can be directly attributable to unsteady aerodynamic characteristics. This can be expected for real-world measurements in complex conditions. Regardless of the difficulty in their interpretation, these results are presented as they may be useful for comparison to future wind-tunnel or numerical aerodynamic investigations of freight trains.

### 3.5. Correlation

Analysis of the cross-correlation of the velocity fluctuations between the probes at different positions provides insight into the existence and scale of coherent flow structures. Such analysis is also useful to infer the influence that the loading configuration has on the flow field, in contrast to the ambient wind. In this section, correlation analysis over the middle 40% section of train T1 is presented for the different velocity components. The results are representative of the low crosswind trains (T1, T2, T3).

In Fig. 25, the cross-correlation of probe P1 (closest to the train,  $y = 1.71$  m) with each of the probes (P1–P7) in rake R1 is presented for the  $u$  velocity component. As expected, moving away from the train, reducing correlation is visible. The correlation coefficient,  $\rho$ , decreases from a relatively high value ( $\rho = 0.6$ ) over a short distance ( $\Delta y = 1$  m), to a relatively low value ( $\rho = 0.2$ ) at the largest distance ( $\Delta y = 6$  m). Similarly, an increasing time-lag exists moving away from the train before the

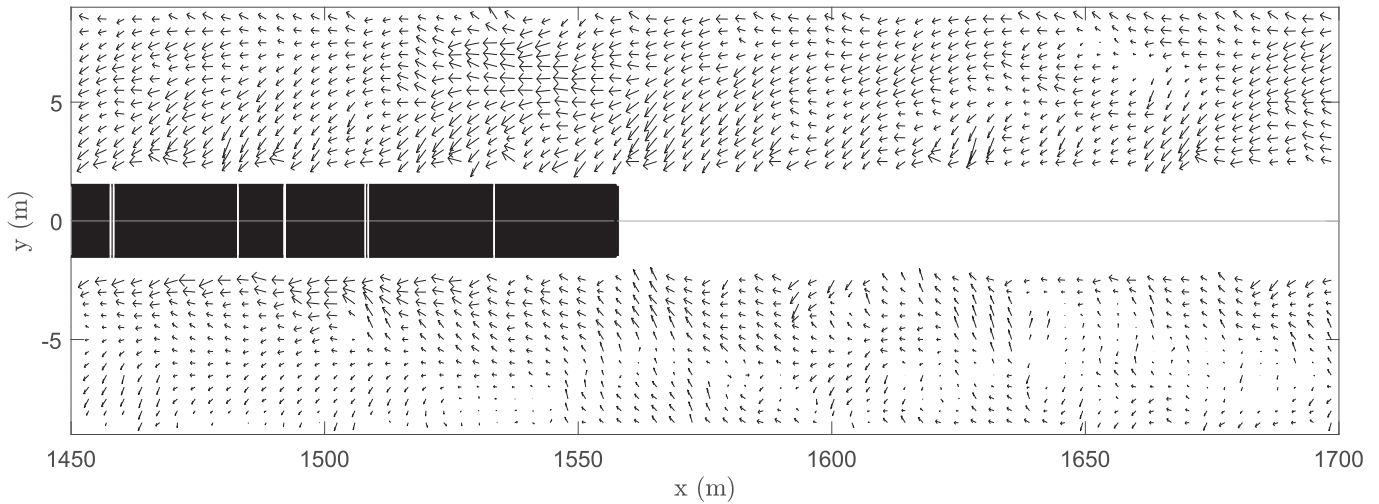


Fig. 23. Velocity vectors of  $u, v$ , around train T1 over the section  $x = 1450\text{--}1700$  m, where the train tail is visible. Train indicated by black box and gaps by white spaces.

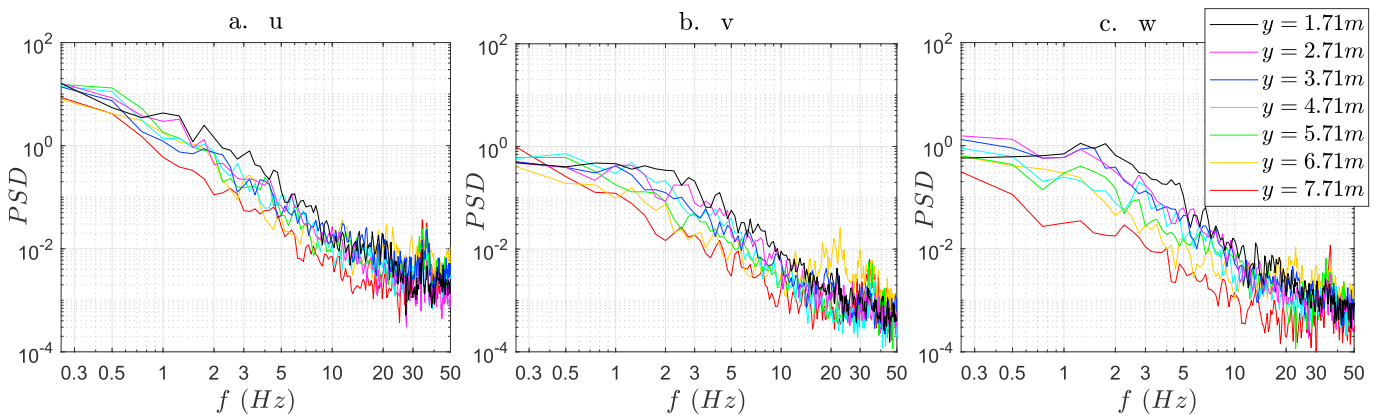


Fig. 24. Power spectral density (PSD) determined from Fast Fourier Transform (FFT) of the different velocity components: (a)  $u$ , (b)  $v$ , (c)  $w$  measured by probes P1–P7 from rake R1, taken over the middle %40 section of train T1.

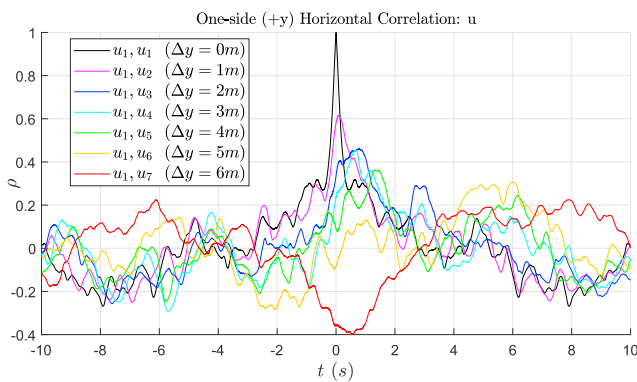


Fig. 25. Cross correlation of the longitudinal velocity,  $u$ , measured over the middle 40% section of train T1 by each probe (P1–P7) in the horizontal rake R1, with P1, presented in terms of the correlation coefficient,  $\rho$ .

probes exhibit their highest correlation. This time-lag is perhaps expected for the close probes (e.g.  $t < 1.7$  s for  $\Delta y < 4$  m), however, it increases significantly for  $\Delta y = 5$  m and  $\Delta y = 6$  m, to considerable time-lags of  $t \approx 5$  s and  $\approx 8$  s (corresponding to  $x \approx 240$  m) respectively. These findings are supported by the results in Fig. 18, where a fluctuation or feature in

the velocity close to the train only convects to the furthest measurement position after a longitudinal length in the range of  $x \approx 240$  m.

Correlation in the transient flow field either side of the train would indicate the loading configuration has a significant effect on the flow field, as its influence is expected to be symmetric, affecting both sides at the same time. In contrast, cross-wind is expected to reduce symmetric in-phase correlation. Symmetric horizontal correlation was investigated by calculating the cross-correlation between the respective probes in rakes R1 and R2 on either side of the train (e.g. R1, P1 ( $y = 1.71$  m) to R2, P1 ( $y = -1.71$  m)). The results for the  $u$  velocity component are presented in Fig. 26. The probes close to the train ( $y = 1.71, 2.71, 3.71$  m) exhibit reasonably high correlation with each other ( $\rho \approx 0.4$ ). However, the two probes at  $y = 2.71$  and  $3.71$  m exhibit the highest correlation for a time-lag of  $\pm 1$  s, indicating that already at these distances, the ambient crosswind may be skewing the flow. Negligible correlation was apparent for the  $v$  and  $w$  velocity components for either the symmetric or one-sided horizontal correlation analysis.

Longitudinal correlation was analysed using the measurements made at the different rakes (R1, R3, R4) on the same side ( $+y$ ) of the train. This enabled two cases with  $\Delta x = 15$  m (R1–R2, R3–R4) and one case of  $\Delta x = 30$  m (R1–R4) to be analysed. The autocorrelation of R1 probes with themselves were also calculated, and all cases are presented in Fig. 27 for the four horizontal probe positions closest to the train. The  $u$  component of velocity is only presented here, as the  $v$  and  $w$  components exhibited negligible correlation.

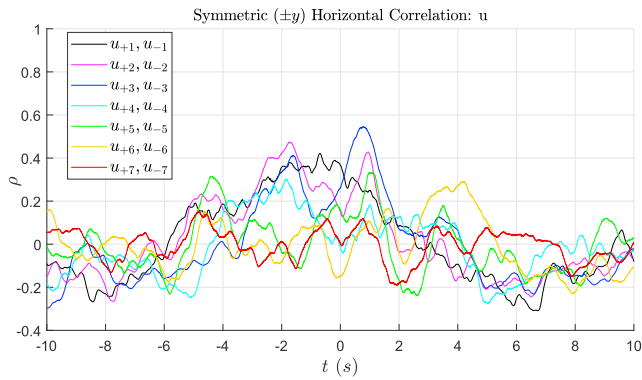


Fig. 26. Cross correlation of the longitudinal velocity,  $u$ , measured over the middle 40% section of train T1 by each probe (P1–P7) in the horizontal rake R1 (+  $y$ ) to its corresponding probe (P1–P7) on the other side of the train in rake R2 (–  $y$ ).

If the flow field around the train were steady over time, high levels of correlation would exist with time-lags corresponding to their distances relative to each other at the test-site divided by the train velocity ( $t = \Delta x/u_t = 0.5$  &  $1$  s when  $\Delta x = 15$  &  $30$  m, respectively). However, this is not observed in the results. Distinct peaks in correlation coefficient of  $\rho \approx 0.4$  are visible for both longitudinal distances; however, they are not consistent across the different horizontal positions. In spite of this inconsistency, a trend is visible of increasing time-lag moving away from the train in the horizontal direction. Even at the closest position,  $y = 1.71$  m, the time-lag of  $\approx 1$  s is greater than the estimated lag of  $0.5$  s using distance and train speed. This increasing time-lag indicates that transient flow structures are generated at the train and then convect away with reducing velocity. The remaining velocity fluctuations not contributing to the  $\rho \approx 0.4$  correlated flow could be attributed to additional transient features in the flow, as well as the effect of transient crosswinds.

4. Conclusions

The boundary layers that develop on the sides of full-scale operational inter-model freight trains have been measured at a test-site set-up situated around a single standard-gauge rail in Victoria, Australia. Rakes of 4-hole dynamic-pressure probes were utilized to measure the velocity induced by passing trains, enabling calculation of the boundary layer characteristics, as well as providing insight into the transient flow

topology around a set of six trains.

The *characteristic boundary layer* – an average boundary layer that occurs at the approximate middle of freight trains operating within low ambient wind ( $\beta < 2^\circ$ ) – was determined to have: a displacement thickness of  $\delta^* = 1.6$  m (within a range of  $\delta^* = 0.5$ – $3$  m), a turbulence intensity profile ranging from 4 to 13% with relatively consistent anisotropy ratios of  $I_u : I_v : I_w \approx 1 : 0.4 : 0.6$ , and turbulent length-scales in the range 5–30 m. This characteristic boundary layer and its additional salient features are illustrated in Fig. 28; it is intended to help inform future experiments and simulations, in order to model real-world conditions experienced by moving freight trains.

Even relatively low ambient-wind conditions (with relative yaw angles  $\beta < 2^\circ$ ) were observed to have an effect on the boundary layer and flow topology at the two sides of a train. Measurements taken either side of the trains exhibited differences in the calculated displacement thickness – and corresponding agreement for multiple measurements taken on the same side of the train – as well as visible asymmetry in the flow topology. These results are not expected to be caused by the loading configuration of the vehicles, and thus can be attributed to the (albeit weak) mean and fluctuating components of the ambient wind.

Loading configuration was found to only have a noticeable influence on the displacement thickness and flow topology when a series of consecutive gaps ( $> 2$  m) between shipping containers existed. This loading configuration led to a reduction in displacement thickness and the bulk induced flow around the train, as one would expect. A measure of the cumulative blockage of the trains was shown to be useful in visualising the loading configuration and exhibited the same trends in the large-scale variation of the displacement thickness profile along the freight trains. No single gap, in spite of significant sizes ( $> 10$  m), was observed to have an observable/measurable effect on either the flow field or displacement thickness, at least in the measurement region away from the train side surfaces (the first probe was located at 1.7 m from the train of width 2.1 m).

The rakes of 7 probes either side of the train provided some insight into transient flow field around the train. Following rapid development of the boundary layer over the first 200 m, the average flow field at the middle of the trains exhibited longitudinal velocities of  $u = 0.4u_t$  (40% of the train speed) and flow towards the train surface of  $v = 0.1u_t$  at  $y = 1.71$  m from the surface, reducing to  $u = 0.1u_t$  &  $v = 0.02u_t$  respectively at  $y = 7.71$  m away from the surface. Fluctuations in longitudinal velocity, caused by large-scale turbulent structures were observed to convect away with reducing velocity from the train surface and downstream. This was evident in the velocity coloured contours and identified

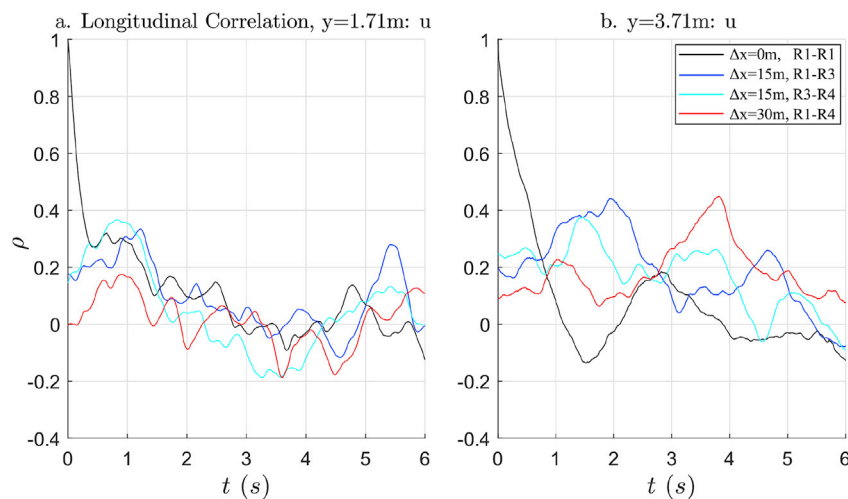


Fig. 27. Cross correlation of the longitudinal velocity,  $u$ , measured over the middle 40% section of train T1 over different longitudinal distances:  $\Delta x = 0$  m (R1–R1),  $\Delta x = 15$  m (R1–R3, R3–R4),  $\Delta x = 30$  m (R1–R4), from different corresponding probes. (a) P1 ( $y = 1.71$  m) and (b) P3 ( $y = 1.71$  m) in each of the different rakes: R1, R3, R4, on the same side of the train (+  $y$ ).

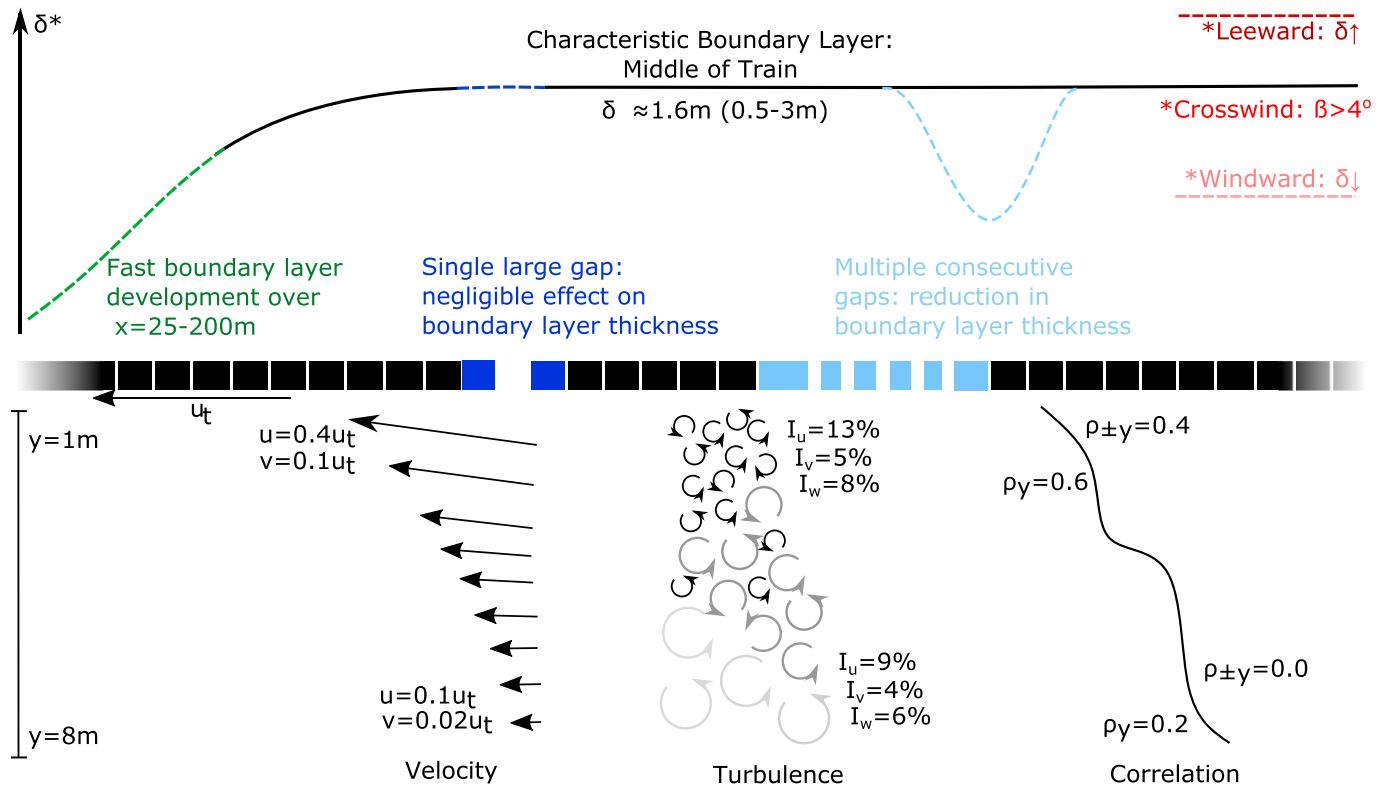


Fig. 28. Salient features of the characteristic boundary layer around an operational inter-modal freight train.

in the horizontal and longitudinal correlation analysis. Further, the transient flow was seen to be somewhat correlated either side of the train, with maximum correlation coefficients of  $\rho = 0.4$  recorded closest to the train ( $\pm y = 1.71$  m) reducing to  $\rho = 0$  away from the train ( $\pm y = 7.71$  m). This symmetric horizontal correlation is expected to be caused by the loading configuration influencing the flow topology. Frequency analysis was performed, however clear dominant frequencies were not evident, with the results being difficult to interpret due to the relative motion of the experiment.

Higher crosswinds ( $\beta = 4-10^\circ$ ) resulted in the flow field on the windward side of the train being pushed close to the surface beyond the reach of the measurement equipment. On the leeward side of the train, signs of the three-dimensional flow field consisting of system of longitudinal vortices forming from separation at the trailing edges of the train and containers were observed, but it was not possible to clearly characterise these due to their complexity and lack of measurement resolution. This resulted in significantly larger bulk induced flow on the leeward side of the train with larger velocities than observed in low crosswind conditions.

The findings presented from this novel experiment: characterising and quantifying the boundary layer structure, and providing insight into the transient flow topology around freight trains, together provide aerodynamic characteristics of typical inter-modal freight trains operating in open air under low crosswind conditions.

The sample size of six trains is acknowledged to be relatively small, even considering that each train is effectively measured three times by each of the horizontal boundary-layer rakes. However, these are the first measurements attempting to spatially and temporally resolve the boundary layers of freight trains operating in real-world conditions. The corresponding results provide (even with variation between different trains as well as along each train's length) an indication of boundary-layer characteristics representative of real-world freight trains that are significantly different than what is typically modelled in wind-tunnel and numerical simulations. These results provide valuable insight that can be useful for comparative aerodynamic investigations on inter-modal freight train aerodynamics in the future.

**Declaration of competing interest**

The authors declare that they have no known competing financial interests or personal relationships that could have appeared to influence the work reported in this paper.

**Acknowledgements**

This research was supported through Pacific National Rail, specifically Michael Kost and Tony McGreevy, and the Australian Research Council's Linkage Project funding scheme, under project number LP13100953. The Australian Rail Track Corporation, notably Sean Adams, are acknowledged for enabling access to the rail corridor. Track force protection services were provided by Paul Jerman from Rail Operations Consulting and Lindsay Hauesler from Aspect Rail. Support from the Monash Wind Tunnel Platform technical staff is acknowledged, specifically Senior Technical Officer Greg Hewes for his extraordinary contribution to the development of the experimental setup, and undertaking of the measurements in challenging conditions.

**References**

Baker, C., 2010. The flow around high speed trains. *J. Wind Eng. Ind. Aerod.* 98, 277–298.  
 Beagles, A., Fletcher, D., 2013. The aerodynamics of freight: approaches to save fuel by optimising the utilisation of container trains. *Proc. IMechE Part F: J. Rail Rapid Transit.* 227 (6), 635–643.  
 Bell, J., Burton, D., Thompson, M., Herbst, A., Sheridan, J., 2015. Moving model analysis of the slipstream ad wake of a high-speed train. *J. Wind Eng. Ind. Aerod.* 136, 127–137.  
 Bell, J., Burton, D., Thompson, M., Herbst, A., Sheridan, J., 2016a. Dynamics of trailing vortices in the wake of a generic high-speed train. *J. Fluid Struct.* 65, 238–256.  
 Bell, J., Burton, D., Thompson, M., Herbst, A., Sheridan, J., 2016b. Flow topology and unsteady features in the wake of a generic high-speed train. *J. Fluid Struct.* 61, 168–183.  
 Bell, J., Burton, D., Thompson, M., Herbst, A., Sheridan, J., 2017. A wind-tunnel methodology for assessing the slipstream of high-speed trains. *J. Wind Eng. Ind. Aerod.* 166, 1–19.

- Bell, J., Burton, D., Thompson, M., Herbst, A., Sheridan, J., 8-11 December, 2014. The effect of length to height ratio on the wake structure and surface pressure of a high-speed train. In: 19th Australasian Fluid Mechanics Conference. AMFC, Melbourne, Australia.
- Bergh, H., Tijdeman, H., 1965. Theoretical and Experimental Results for the Dynamic Response of Pressure Measuring Systems. National Aero and Astronautical Research Institute, Amsterdam, 328(Report NLR-TRF).
- Buhr, A., Ehrenfried, K., 2017. High-speed particle image velocimetry of the flow around a moving train model with boundary layer control elements. *Int. J. Mech. Aerospace Industr. Mechatr. Manuf. Eng.* 11 (3), 47–55.
- CEN, 2013. European Committee for Standardization. Railway Applications - Aerodynamics ÁC<sup>+</sup> Part 4: Requirements and Test Procedures for Aerodynamics on Open Track, CEN EN 14067-4.
- Cooper, K., Campbell, W., 1981. An examination of the effects of wind turbulence on the aerodynamic drag of vehicles. *J. Wind Eng. Ind. Aerod.* 9, 167–180.
- Copley, J., 1987. The 3-d flow around railway trains. *J. Wind Eng. Ind. Aerod.* 26.
- Engdahl, R., Gielow, R., Paul, J., 1986. Train resistance - aerodynamics volume i of ii intermodal car application. In: Proceedings of Railroad Energy Technology Conference II. Association of American Railroad, Atlanta, GA, pp. 225–268.
- Flynn, D., Hemida, H., Baker, C., 2016. On the effect of crosswinds on the slipstream of a freight train and associated effects. *J. Wind Eng. Ind. Aerod.* 156, 14–28.
- Flynn, D., Hemida, H., Soper, D., Baker, C., 2014. Detached-eddy simulation of the slipstream of an operational freight train. *J. Wind Eng. Ind. Aerod.* 132, 1–12.
- Gallagher, M., Morden, J., Baker, C., Soper, D., Quinn, A., Hemida, H., Sterling, M., 2018. Trains in crosswinds - comparison of full-scale on-train measurements, physical model tests and cfd calculations. *J. Wind Eng. Ind. Aerod.* 175, 428–444.
- Gielow, M., Furlong, C., 1988. Results of Wind Tunnel and Full-Scale Tests Conducted from 1983 to 1987 in Support of the Association of American Railroads' Train Energy Program. Publication R-685 Association of American Railroads.
- Hemida, H., Baker, C., 2010. Large-eddy simulation of the flow around a freight wagon subjected to a crosswind. *Comput. Fluids* 39, 1944–1956.
- Holmes, J., 2001. Wind Loading of Structures. Spon Press, New York.
- Iberall, A., 1950. Attenuation of Oscillatory Pressures in Instrument Lines. US Department of Commerce National Bureau of Standards, pp. 93–107, 45(RP2115).
- Irwin, H., 1981. The design of spires for wind simulation. *J. Wind Eng. Ind. Aerod.* 7, 361–366.
- Irwin, H., Cooper, K., Girard, R., 1979. Correction of distortion effects caused by tubing systems in measurements of fluctuating pressures. *J. Ind. Aerod.* 5, 93–107.
- Lai, Y.-C., Barkan, C., 2005. A rolling horizon model to optimize aerodynamic efficiency of intermodal freight trains with uncertainty. *Transport. Res. Rec.: J. Transport. Res. Board* 1916, 47–55.
- Lai, Y.-C., Ouyang, Y., Barkan, C., 2008. A rolling horizon model to optimize aerodynamic efficiency of intermodal freight trains with uncertainty. *Transport. Sci.* 42 (4), 466–477.
- Li, C., Burton, D., Kost, M., Sheridan, J., Thompson, M., 2017. Flow topology of a container train wagon submitted to varying local loading configurations. *J. Wind Eng. Ind. Aerod.* 169, 12–29.
- Lukaszewicz, P., 2007. A simple method to determine train running resistance from full-scale measurements. *Proc. IMechE Part F: J. Rail Rapid Transit.* 221, 331–338.
- Lukaszewicz, P., 2009. A simple method to determine train running resistance from full-scale measurements. *Proc. IMechE Part F: J. Rail Rapid Transit.* 223, 189–197.
- Maleki, S., Burton, D., Thompson, M., 2017. Assessment of various turbulence models (eles, sas, urans and rans) for predicting the aerodynamics of freight train container wagons. *J. Wind Eng. Ind. Aerod.* 170, 68–80.
- Maleki, S., Burton, D., Thompson, M., 2019. Flow structure between freight train containers with implications for aerodynamic drag. *J. Wind Eng. Ind. Aerod.* 188, 194–206.
- McAuliffe, B., Belluz, L., Belzile, M., 2014. Measurement of the on-road turbulence environment experienced by heavy duty vehicles. *SAE Int. J. Commer. Veh.* 7 (2).
- Muld, T., Efraimsson, G., Hennigson, D., 2013. Wake characteristics of high-speed trains with different lengths. *Proc. IMechE Part F: J. Rail Rapid Transp.* 228 (4), 333–342.
- Öngüner, E., Henning, A., Fey, U., Wagner, C., 2020. Towards aerodynamically optimized freight wagons: an experimental study on container designs. In: Dillmann, A., Heller, G., KrÄmmer, E., Wagner, C., Tropea, C., JakirliÄ†, S. (Eds.), *New Results in Numerical and Experimental Fluid Mechanics XII. DGLR 2018. Notes on Numerical Fluid Mechanics and Multidisciplinary Design*, vol. 142, pp. 437–446.
- Östh, J., KrajnoviÄ†, S., 2014. A study of the aerodynamics of a generic container freight wagon using large-eddy simulation. *J. Fluid Struct.* 44, 31–54.
- Paul, J., Johnson, R., Yates, R., 2007. Application of cfd to rail car and locomotive aerodynamics. In: *The Aerodynamics of Heavy Vehicles II: Trucks, Buses and Trains*, pp. 259–297.
- Peters, J., 1993. Effect of Reynolds number on the aerodynamic forces on a container model. *J. Wind Eng. Ind. Aerod.* 49, 431–438.
- Raghunathan, R., Kim, H., Setoguchi, T., 2002. Aerodynamics of high-speed railway train. *Prog. Aero. Sci.* 38, 469–514.
- Shetz, J., 2001. Aerodynamics of high-speed trains. *Annu. Rev. Fluid Mech.* 33, 371–414.
- Sima, M., Tietze, A., Schulz, B., Ehrenfried, K., 2016. Representing large boundary layers in slipstream moving model tests. In: *Railways 2016, the Thirds International Conference on Railway Technology: Research Development and Maintenance*, 05-07 April, Cagliari, Italy.
- Sims-Williams, D., 2011. Cross Winds and Transients: Reality, Simulation and Effects. SAE Technical Paper 01-0172.
- Soper, D., 2014. The Aerodynamics of a Container Freight Train. PhD Thesis. University of Birmingham.
- Soper, D., Baker, C., 2019. A full-scale experimental investigation of passenger and freight train aerodynamics. *Proc. IMechE Part F: J. Rail Rapid Transit.* 1–16, 0(0).
- Soper, D., Baker, C., Sterling, M., 2014. Experimental investigation of the slipstream development around a container freight train using a moving model facility. *J. Wind Eng. Ind. Aerod.* 135, 105–117.
- Sterling, M., Baker, C., Jordan, S., Johnson, T., 2008. A study of the slipstreams of high-speed passenger trains and freight trains. *Proc. Inst. Mech. Eng. Part F: J. Rail Rapid Transp.* 222, 177–193.
- Storms, B., Salari, K., Babb, A., 2008. Fuel Savings & Aerodynamic Drag Reduction from Rail Car Covers, vol. 40, pp. 147–178. AfricaRail, 2-6 June, Johannesburg, South Africa.
- Watkins, S., Cooper, K., 2007. The Unsteady Wind Environment of Road Vehicles: Part Two: Effects on Vehicle Development and Simulation of Turbulence. SAE Technical Paper 1(1).
- Watkins, S., Saunders, J., Kumar, H., 1992. Aerodynamic drag reduction of goods trains. *J. Wind Eng. Ind. Aerod.* 40, 147–178.
- Wordley, S., Saunders, J., 2008. On-road turbulence. *SAE Int. J. Passeng. Cars - Mech Syst.* 1 (1).